Timing of formation and exhumation of the Montagne Noire double dome, French Massif Central

Françoise Roger [a,*], Christian Teyssier [b], Jean-Patrick Respaut [a], Patrice F. Rey [c], Marc Jolivet [d], Donna L. Whitney [b], Jean-Louis Paquette [e], Maurice Brunel [a]

[a] Laboratoire Géosciences Montpellier (CNRS-UMR 5243), Université Montpellier 2, 34095 Montpellier Cedex 5, France
[b] Department of Earth Sciences, University of Minnesota, Minneapolis, MN 55455, USA
[c] School of Geosciences, The University of Sydney, Sydney, NSW 2006, Australia
[d] Laboratoire Géosciences Rennes (CNRS-UMR 6118), Université Rennes 1, Campus de Beaulieu, 35042 Rennes, France
[e] Laboratoire "Magmas et Volcan" (CNRS-UMR 6524), Université B. Pascal, F-63 038 Clermont-Ferrand Cedex, France

ARTICLE INFO

ABSTRACT

New U–Pb monazite, zircon, and xenotime ages date the Late Carboniferous crystallization of the anatectic Vialais granite in the Montagne Noire Axial Zone and the high-temperature deformation and metamorphism of the augen gneiss (Ordovician granite protolith) from which the granite was likely derived. The U–Pb monazite ages obtained from the augen gneiss (308 ± 3 Ma), late kinematic Vialais granite (303 ± 4 Ma), and post-kinematic leucogranite (298 ± 2 Ma), bracket the high-temperature deformation and metamorphism at ~310–300 Ma, clearly postdating regional contraction and nappe emplacement (>320 Ma). The planar–linear and locally linear fabrics in the augen gneiss outline a regional-scale double dome structure (Caroux and Espinouse sub-domes) containing smaller (km-scale) upright folds. Compared to the Caroux sub-dome, the larger, migmatitic Espinouse sub-dome contains abundant leucosome, leucogranite bodies and late-kinematic intrusions (Vialais granite). The Vialais granite displays a weak magmatic foliation that defines the main layering of the Espinouse migmatite. Ellipsoidal quartz–sillimanite nodules concentrated above the roof of the granite recorded an increment of strain (vertical shortening, E–NE elongation) during granite emplacement and crystallization, consistent with the extension event that exhumed the domes. These new geochronological and structural data suggest that the Montagne Noire double dome formed in a pull-apart structure within a dextral strike–slip system. Upright folding in the sub-domes has been traditionally assigned to a regional contraction event; alternatively, we propose that local contraction is associated with the convergence of low-viscosity crust beneath the upper crust pull-apart. Dynamic models of extension of hot crust indicate that contraction at depth is generated by flow of low-viscosity orogenic crust converging and rising to fill the gap created by upper crust extension. This interpretation solves the long-standing problem of apparent coeval contraction and extension in the Montagne Noire double dome and establishes migmatite dome emplacement in strike–slip corridors as a style of late Variscan tectonics.

1. Introduction

Exhumed high-grade metamorphic rocks, including migmatites that represent crystallized partially molten crust, provide a record of the mechanisms, trajectory, magnitude, and timing of crustal flow during the construction and collapse of orogens (e.g., Brown, 1994, 2001; Ledru et al., 2001; Vanderhaeghe and Teyssier, 2001; Teyssier and Whitney, 2002; Rey et al., 2001; Rosenberg and Handy, 2005; Vanderhaeghe, 2009, 2012; Gordon et al., 2008, 2009; Kruckenberg et al., 2008, 2011; Whitney et al., 2004, 2013). Exhumation of weak lower crust commonly occurs at the edges of orogens and can be driven by intense erosion (Beaumont et al., 2001, 2006) or by extension/transtension (e.g., Teyssier et al., 2005; P.F. Rey et al., 2009; Rey et al., 2011a,b). Recognizing the primary mechanisms of exhumation relies on documenting the timing of crystallization and cooling of low-viscosity crust in the context of the structural evolution of the flowing crust and its surroundings.

In this paper, we explore the timing and mechanism of exhumation of the high-grade core (Axial Zone) of the Montagne Noire, a segment of the Variscan belt located at the southern edge of the French Massif Central (Fig. 1). The Axial Zone consists of two elongate sub-domes that together create a double dome of gneiss (in part migmatitic). The double-dome is surrounded by a carapace of schist that exhibits decreasing metamorphic grade with increasing distance from the gneiss dome, as well as low-grade tectonic nappes and sedimentary basins (Fig. 1).

* Corresponding author.
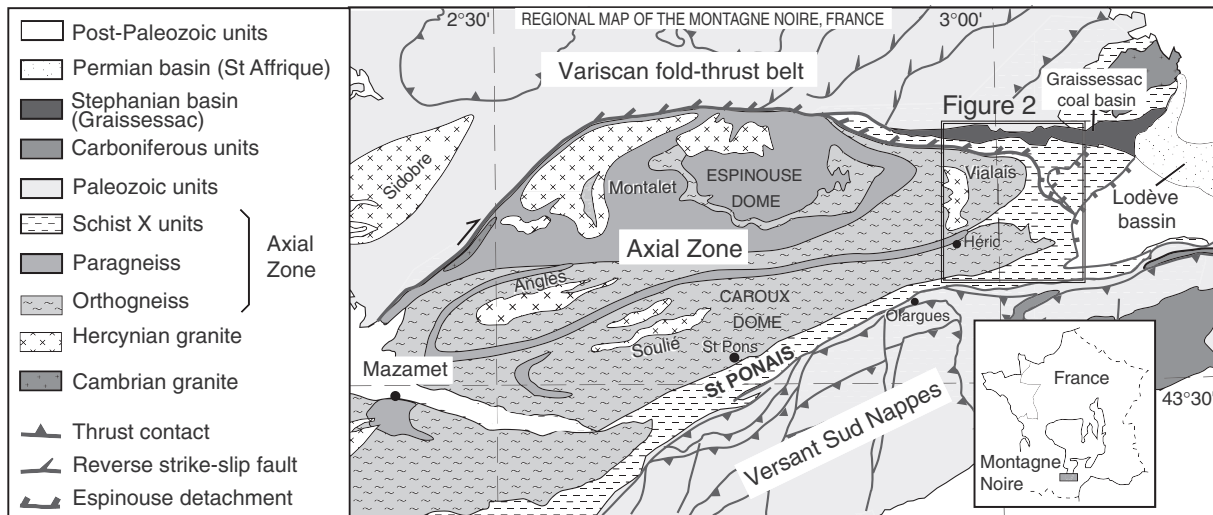E-mail address: Francoise.Roger@gm.univ-montp2.fr (F. Roger).

Fig. 1. Regional map of the Montagne Noire double dome, showing the northern fold-thrust belt, the Axial Zone, including the Espinouse and Caroux domes, and the "Nappes duVersant Sud". The Vialais granite is located at the eastern end of the Espinouse dome; area covered in Fig. 2 is outlined.

The mode of exhumation of the high-grade core of the Montagne Noire has been debated for many decades. It has been attributed to diapirism (Gèze, 1949; Schuiling, 1960; Faure et al., 2010) as well as contractional/transpressional (Arthaud, 1970; Matte et al., 1998; Demange, 1999; Matte, 2007; Malavieille and Konstantinoskaya, 2010), strike–slip (Nicolas et al., 1977; Franke et al., 2011), and extensional/transtensional tectonics (Van den Driessche and Brun, 1989, 1992; Echtler and Malavieille, 1990; Brun and Van den Driessche, 1994, 1996; Rey et al., 2011a,b). One reason for this wide range of models is uncertainty surrounding the timing of emplacement of the Axial Zone in relation to the regional sequence of contraction and extension events. Dating the dome-forming event (flow of gneiss and migmatite) in relation to the crystallization of partial melt and granite bodies — combined with structural data from the granite and gneiss — sheds considerable light on the mechanisms of dome formation and the tectonic context in which the dome formed.

Here we report new U–Pb zircon and monazite ages for a prominent granite body (Vialais granite) that has been used to evaluate the age of the last stages of melt crystallization in the Montagne Noire Axial Zone (e.g., Matte et al., 1998; Faure et al., 2010). Our new dates for the Vialais granite are at least 20 m.y. younger than previously published ages and therefore reopen the interpretation of the geodynamic context in which the Montagne Noire dome developed. We also report new U–Pb zircon and monazite ages of the classic augen gneiss of the Montagne Noire Axial Zone; these ages along with field relationships indicate that the Vialais granite was likely derived from partial melting of the augen gneiss and that the flow of dome rocks is younger than previously suggested. We discuss these results in the context of published numerical models (e.g., Rey et al., 2011a,b) for the formation of "double" gneiss/migmatite domes such as the Montagne Noire.

2. Overview of the Montagne Noire

The Montagne Noire is part of the Variscan belt and is located at the southern edge of the French Massif Central (Fig. 1). It is classically described as consisting of three main units (Figs. 1, 2). The northern unit is a SW-directed thrust imbricate involving low-grade lower Paleozoic metasedimentary strata. The central unit (Axial Zone) mainly comprises migmatitic orthogneiss (augen gneiss) within two elongate domes trending ENE–WSW, the Espinouse and Caroux domes. The Axial Zone also includes minor micaschist, marble/calc-silicate, and mafic to ultramafic layers and pods; at a few localities mafic pods display eclogite-facies assemblages (Demange, 1985; Faure et al., 2014).

The southern unit of the Montagne Noire consists of the "Nappes du Versant Sud", in which Paleozoic cover sequences are involved in km-scale recumbent fold nappes (Arthaud, 1970). The Carboniferous emplacement age of these nappes has been bracketed by biostratigraphic relations at 335–325 Ma (Engel et al., 1980; Feist and Galtier, 1985), although an age <320 Ma has also been proposed based on stratigraphic considerations (Franke et al., 2011). In a recent paper Doublier et al. (2014) argue, based on low-grade petrology and K–Ar geochronology, that the Versant Sud nappes preserve medium pressure metamorphism away from the Axial Zone; this metamorphism is 20 million years older than the 310–300 Ma high temperature overprint that dates the emplacement of the dome in the Axial Zone in a transtensional setting.

In the Axial Zone, the western closure of the dome is outlined by the contact between micaschist and gneiss (Demange, 1982) (Fig. 1). At the eastern end of the dome the Espinouse and Caroux sub-domes are separated by a tight synform of micaschist (Rosis syncline; Fig. 2). Metamorphic grade has been documented in the micaschist envelope in the eastern part of the Axial Zone (Bard and Rambeloson, 1973; Thompson and Bard, 1982) and in the gneissic core (Schuiling, 1960, 1963; Schuiling and Widt, 1962; Den Tex, 1975; Demange, 1982; Soula et al., 2001). Results point to a late low P–high T metamorphic evolution associated with the development of widespread partial melting and shallow emplacement of Late Variscan granitoids (some cordierite-bearing), including the Vialais granite, which is generally concordant but locally crosscuts augen gneiss foliation and lineation (e.g. Bogdanoff et al., 1984) (Fig. 1).

3. Structure of the Axial Zone of the Montagne Noire

In the eastern part of the Montagne Noire, the southern (Caroux) sub-dome is well exposed along the classic section of the Gorges d'Héric (Fig. 2A) and consists primarily of augen gneiss, with K-feldspar augen several centimeters in size (Fig. 3A). The augen gneiss typically has a well-defined foliation that can be traced around kilometer-scale upright folds (Fig. 2B). The gneiss fabric is planar–linear in the fold limbs and is dominantly linear (L-tectonite) in the fold hinges, suggesting that folding and fabric development were synchronous, at least in part. Foliation orientation varies according to position in the folds, and lineation is consistently oriented E–W, parallel to fold hinges.

The augen gneiss is also the host of thin layers (up to a few tens of meters) of fine-grained gneiss that are also zones of high-strain (mylonite). The fine-grained gneiss units can be mapped continuously and are
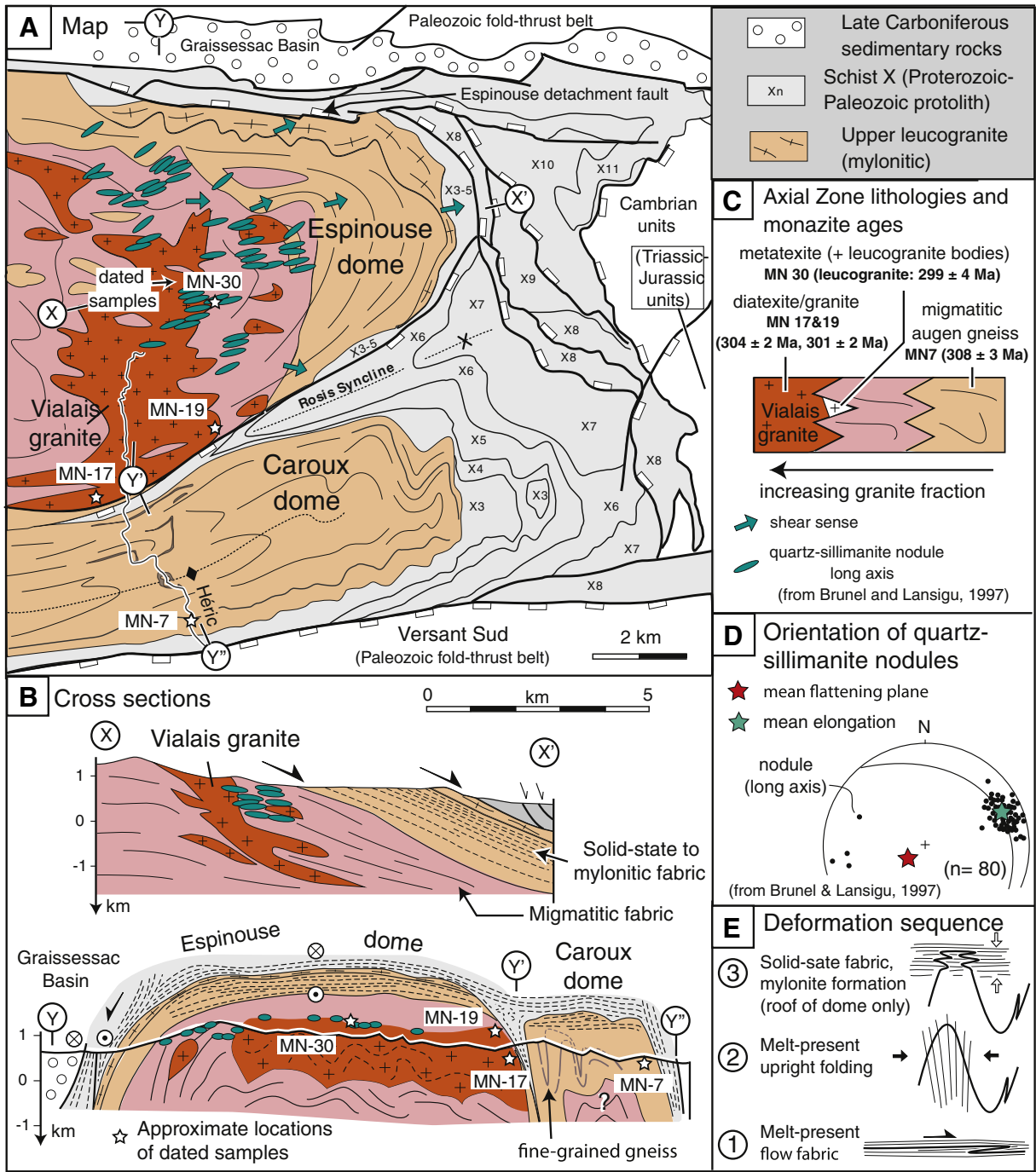
Fig. 2. A) Detailed map of the eastern termination of the Montagne Noire double dome (see Fig. 1 for location); ellipses indicate the orientation of quartz–sillimanite nodules; B) X–X′ and Y–Y′–Y″ (Fig. 1A) cross-sections of the Axial Zone, showing the double dome geometry and the diffuse outline of the Vialais granite. C) Schematic section of progressive changes from augen gneiss to diatexite migmatite with ages from this study. D) Stereonet plot (lower hemisphere) of long and short axes of sillimanite nodules (Brunel and Lansigu, 1997). E) Interpretation of structural sequence in the Axial Zone of the Montagne Noire. Sample coordinates: MN 17 (43°35′59″N; 2°56′28″E)–MN19 (43°36′42″N; 2°58′08″E)–MN 30 (43°38′23″N; 2°58′08″E)–MN7 (43°34′49″N; 2°58′02″).

involved in the kilometer-scale folds defined by the augen gneiss foliation (Fig. 2A, B). The fine-grained gneiss hosts lithologically varied bodies such as calc-silicate and mafic and ultramafic pods, including amphibolite and eclogite (Faure et al., 2010).

In the northern (Espinouse) sub-dome, Caroux-type augen gneiss is preserved at the eastern periphery of the dome and becomes increasingly migmatitic downward, toward the core of the dome (Fig. 2). With increasing structural depth, the augen gneiss develops a layering that includes an increasing fraction of leucosome (metatexite) and larger garnet-bearing leucogranite bodies (Fig. 3B) several tens of meters

thick (Beaud, 1985), and grades into biotite granite (Vialais granite; Bogdanoff, 1970). Whereas the migmatitic augen gneiss shows a well-developed foliation and lineation, the Vialais granite contains a weak magmatic foliation defined by alignment of biotite grains and aggregates (Fig. 3C); this foliation is roughly concordant with the regional foliation of the migmatite. Like in the Caroux sub-dome, the foliation of the Espinouse migmatite is folded around km-scale upright folds (Bogdanoff et al., 1984) (Fig. 2B).

The high melt-fraction (diatexite) migmatite that includes the Vialais granite is characterized by the common occurrence of quartz-

Fig. 3. A) The Héric augen gneiss (sample MN7). B) Undeformed garnet-bearing leucogranite (sample MN 30) near the Ourtigas Pass. C) The Vialais granite (sample MN 19) consists of quartz, K-feldspar, biotite, muscovite, and garnet. D) Vialais granite with quartz–sillimanite nodules near the Ourtigas Pass.

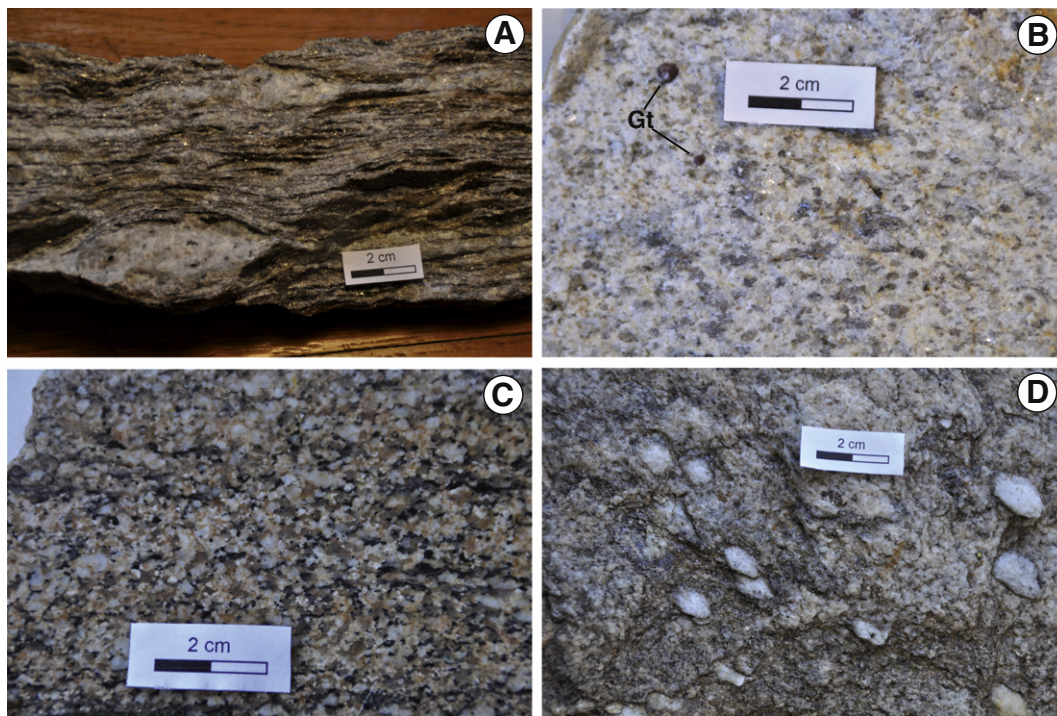sillimanite (fibrolite) nodules (Fig. 3D) concentrated at the roof of the Vialais granite (Bogdanoff, 1970; Loueyit, 1978; Beaud, 1985; Brunel and Lansigu, 1997). These ellipsoidal nodules are typically 1–3 cm in their long dimension and are spaced up to a few tens of cm in the folia-tion plane; the aspect ratio of the nodules long/short axes is typically between 2 and 10, with a majority of ratios around 4–5 (Beaud, 1985). The nodules' long axes are oriented in the E–NE direction and the short axes are close to vertical (Fig. 2D). Overall, the nodules ellipsoidal shapes indicate deformation close to plane strain with a slight compo-nent of flattening, particularly in the more micaceous migmatitic gneiss (Beaud, 1985). The flattening plane of the nodules is close to horizontal (shallow dip to the E–NE) and is typically oblique to the more steeply dipping migmatite foliation. This relation has led to the interpretation that the quartz–sillimanite nodules formed during the crystallization of the Vialais granite and deformed during a strain increment involving vertical shortening and horizontal extension in a fluid-rich system (Brunel and Lansigu, 1997). According to this hypothesis, significant de-formation of the migmatite ceased after this increment of deformation.

The migmatitic core of the Espinouse sub-dome and the high-temperature fabric of the Caroux augen gneiss are progressively overprinted upward by a nearly flat melt-present to solid-state fabric that grades into a mylonitic fabric and forms the carapace of the domes (Fig. 2A, B). The metamorphic grade of this strong fabric decreases rapidly upward into the Schistes X units (Fig. 2) in a manner similar to core complex detachment shear zones (Van den Driessche and Brun, 1989, 1992; Echtler and Malavieille, 1990; Brun and Van den Driessche, 1994, 1996). The northern and eastern margins of the Espinouse sub-dome as well as the eastern termination of the Caroux sub-dome consist of normal sense shear zones that have accommodated the Axial Zone exhumation. Timing of this extension event has been associated with deposition of the Late Carboniferous (Stephanian) Graissessac basin and cooling of the Axial Zone core through the argon closure temperature of biotite and white mica (Maluski et al., 1991).

In summary, the high-temperature structural evolution of the Montagne Noire includes a migmatitic layering, presumably flat-lying, that was folded by upright folds within the Caroux and Espinouse sub-

domes; folding also took place in the presence of partial melt. These high-temperature (migmatitic) fabrics were severely overprinted at the roofs of the domes by mylonite zones that cut downward into the dome structures. Although the mylonitic foliation clearly crosscuts the high-grade fabrics at the top of the dome, extensional structures in the upper part of the crust may have developed coevally with ductile flow folding and dome development at lower structural levels.

In this study, we report new zircon, monazite, and xenotime U–Pb ages from four samples that largely span the melt-present history of the Montagne Noire: one in the Caroux augen gneiss (Héric augen gneiss, sample MN7), two in the Vialais biotite granite (MN17, MN19), and one in a garnet-bearing leucogranite body at the roof of the Vialais granite (MN30). We show that the similarity in zircon populations (Figs. 4, 5) identifies the augen gneiss as a likely source for the Vialais anatectic granite. Furthermore, monazite ages (Figs. 6, 7) are grouped around 310–300 Ma for both the augen gneiss and the Vialais granite and associated leucogranite bodies. These results are in contradiction with the recently reported assertion that high-temperature metamor-phism and anatexis in the Montagne Noire is 333–326 Ma in age (Faure et al., 2010, 2014). Consequently our new results demand a new model for the tectonic context in which the Montagne Noire dome was emplaced, one that integrates the progressive deformation recognized in the dome rocks, the emplacement and deformation of anatectic granite, the exhumation history of the dome (structure and cooling), and the Variscan tectonic context of the Montagne Noire dome.

4. Previous geochronology work in the Montagne Noire Axial Zone

The protolith ages for the augen gneiss within the Axial Zone have been determined by U–Pb zircon dating at *ca.* 520 Ma (Ducrot et al., 1979) and *ca.* 450 Ma (Roger et al., 2004). Recent zircon U–Pb ages obtained by Cocherie et al. (2005) and Faure et al. (2010) on other samples from the same area confirm both ages.

Zircon grains of the Héric augen gneiss (sample MN7), for which we report monazite ages here, were dated by the ID-TIMS method (Roger
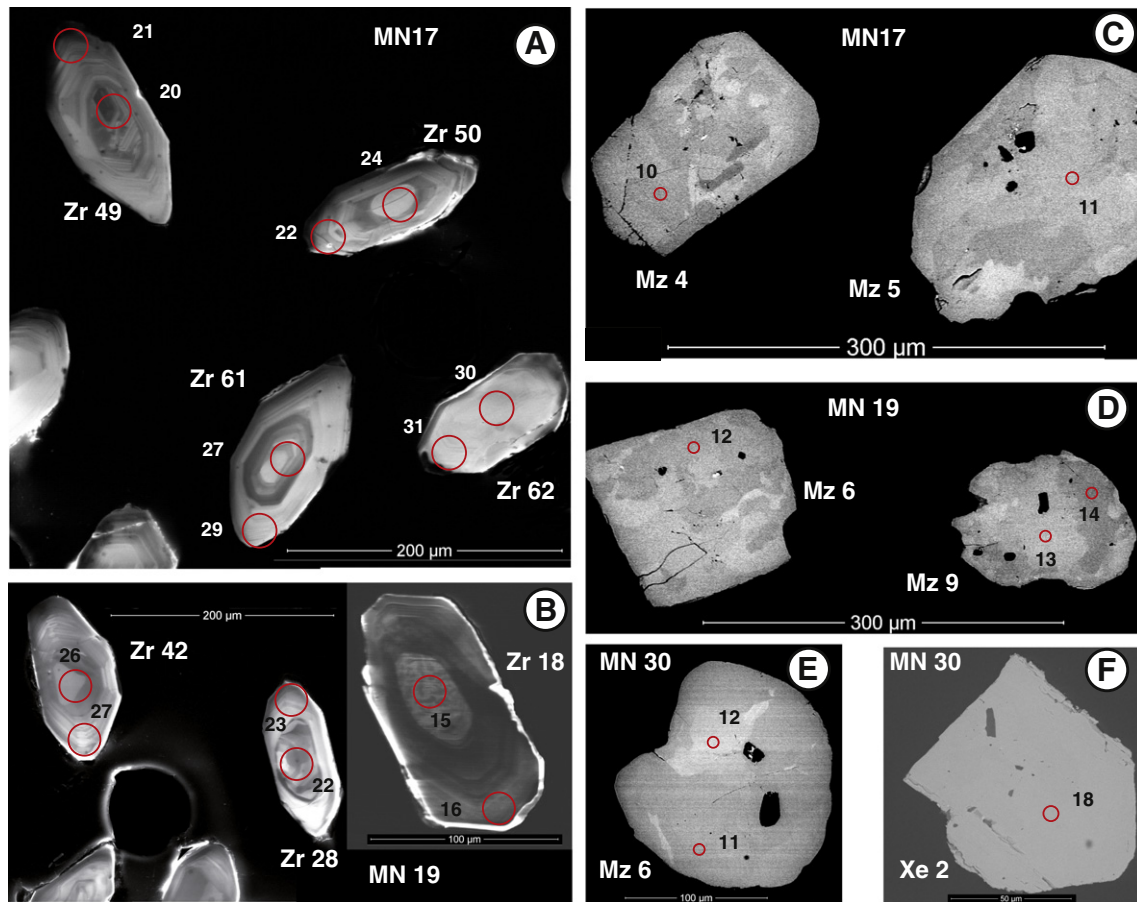
Fig. 4. Cathodoluminescence images of dated zircons, monazites and xenotime crystals. (A) Zircons of the Vialais granite (sample MN17). (B) Zircons of the Vialais granite (sample MN19). (C) Monazite of sample MN17. (D) Monazite of sample MN19. (E) Monazite of the Ourtigas leucogranite (MN30). (F) Xenotime of sample MN30. Circles indicate the analytical spots with a diameter of about 26 μm (zircon) or 7 μm (monazite and xenotime). The numbers refer to analytical data in Table 2 or 3.

et al., 2004). Linear regression of three zircon fractions yielded an upper intercept age of 449.5 ± 7.9 Ma (MSWD = 0.53). The data for the three fractions of zircon have a restricted range of $^{207}Pb/^{206}Pb$ ages, with a weighted average of 450 ± 6 Ma (MSWD = 0.54) (Fig. 5B). This age is similar to the upper intercept age (452 ± 8 Ma, MSWD = 1.02) and $^{207}Pb/^{206}Pb$ age (456 ± 3 Ma, MSWD = 0.76) that were previously obtained by ID-TIMS on zircons of the Pont-de-Larn augen gneiss (sample

MN 15, Roger et al., 2004) collected in the core of the Axial Zone (to the north of the town of Mazamet) (Figs. 1 and 5B).

Based on electron microprobe analyses of monazite (U–Th–Pb), Faure et al. (2010) proposed that the emplacement of anatectic granitoids occurred at 333–326 Ma and the emplacement of late granitoids took place between 325 and 316 Ma, including the Vialais granite (320 ± 3 Ma). These results are similar to the monazite age of 327 ±
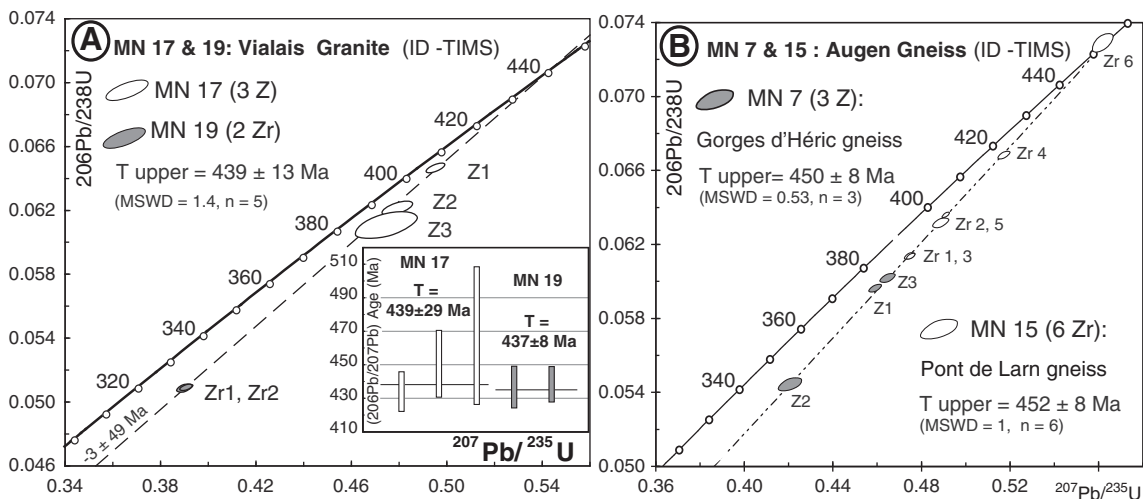
Fig. 5. Zircon U–Pb concordia diagrams obtained with ID-TIMS for the Vialais granite (samples MN 17 and 19). Error ellipses and uncertainties in ages are ± 2σ. (B) Zircon U–Pb Concordia diagram obtained with ID-TIMS for the Héric augen gneiss (Mn7) and Pont-de-Larn augen gneiss (MN15).
B, after Roger et al. (2004).
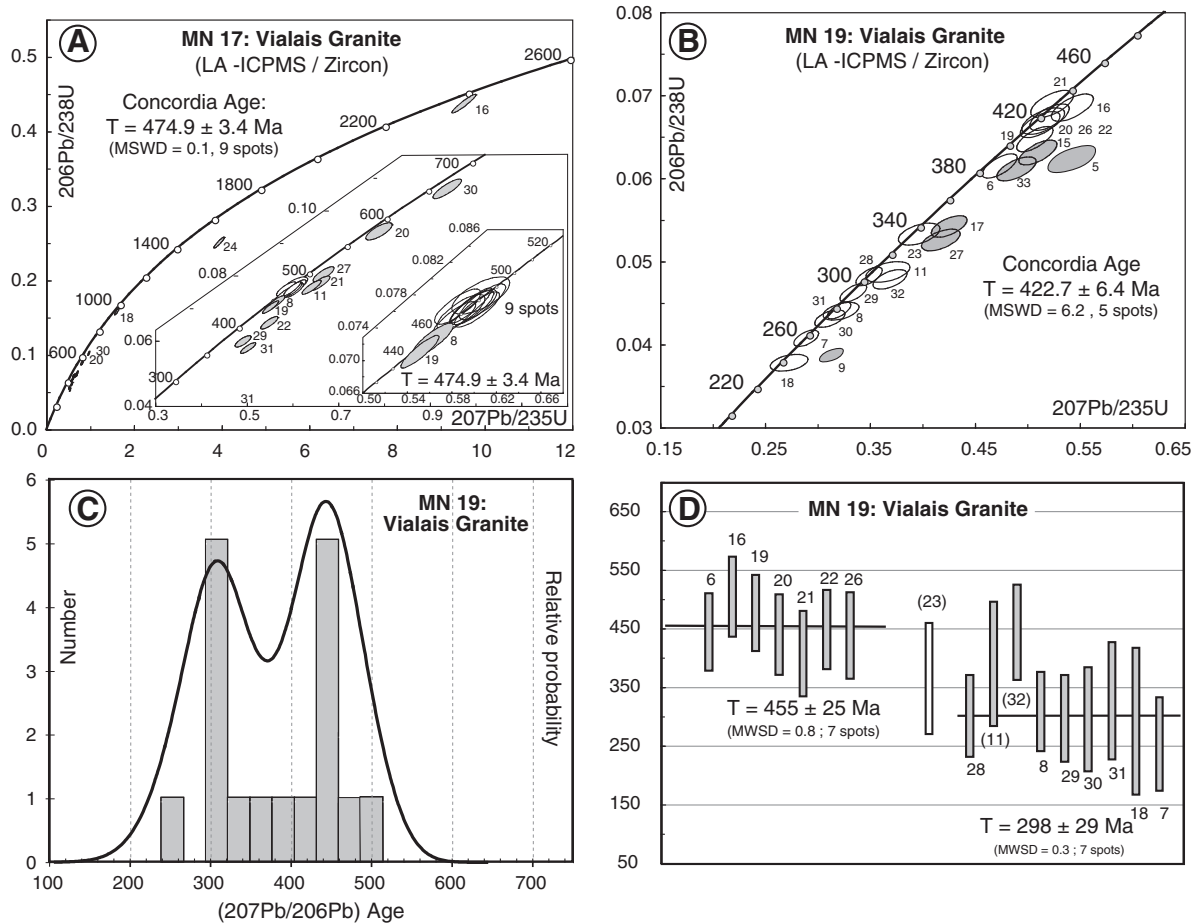
Fig. 6. Zircon U–Pb diagrams obtained with LA-ICPMS for the Vialais granite (MN17 and 19). A and B) Concordia diagrams (samples MN17 and MN19); error ellipses and uncertainties in ages are ±2σ. C) Histogram diagram of concordant ^{207}Pb/^{206}Pb ages (white ellipses in B) for the sample MN19. D) The diagram of the weighted average ^{207}Pb/^{206}Pb ages for the sample MN19.

3 Ma (U–Pb TIMS) that had been previously published for the Vialais granite and that was used to associate the Axial Zone with contraction in the Variscan belt (Matte et al., 1998).

More recently, using TIMS U–Pb dating of zircon and monazite from a foliated aplite dike transposed in the main foliation in the Gorges d'Héric (Caroux sub-dome, Fig. 2), Franke et al. (2011) obtained ages of 309 ± 3 Ma (lower intercept for zircon fractions) and 313 ± 1 Ma (concordant monazite fraction). Younger ages have been obtained on the syntectonic Montalet granite (northern margin of the Espinouse sub-dome, Fig. 1) using the U–Th–Pb LA-ICPMS method (Poilvet et al.,

Fig. 7. Monazite U–Pb diagram obtained with ID-TIMS for the Héric augen gneiss (MN7).

2011): 294 ± 1 Ma (monazite) and 294 ± 3 Ma (zircon). These ages are similar to those obtained on the Saint-Eutrope orthogneiss at the northern edge of the Espinouse dome (Fig. 1). This orthogneiss experienced intense shearing and mylonite development along an extensional detachment (Beaud, 1985) at ca. 295 Ma (U–Th–Pb LA-ICPMS on monazite; Pitra et al., 2012).

Results from K–Ar analyses of muscovite from various rock types and localities in the Montagne Noire show ages ranging from 297 to 292 Ma (Franke et al., 2011). Muscovite from sheared gneiss in the eastern and northern parts of the Axial Zone yielded ^{40}Ar–^{39}Ar ages of 300 ± 3 Ma (Caroux) and 297 ± 3 Ma (Espinouse), respectively (Maluski et al., 1991). Biotite in the same Caroux sample yields an age of 316 ± 4 Ma that is older than the muscovite age. Muscovite and biotite from two separate samples of "banded gneiss" from the southern margin of the Caroux sub-dome yielded 309 ± 3 Ma and 308 ± 3 Ma, respectively (Maluski et al., 1991). Fabric-forming muscovite flakes extracted from a Devonian marble (Nappes du Flanc Sud) in proximity to the Caroux sub-dome yielded an age of 297 ± 3 Ma; this has been interpreted as the age of deformation and dynamic recrystallization of marble at the base of the southern nappes during dextral shearing along the southern margin of the Caroux dome (Maluski et al., 1991).

5. New U–Pb dates for the Caroux augen gneiss and the Vialais granite

5.1. Studied samples

One sample of augen gneiss (MN 7) was collected along the path in the Gorges d'Héric, by the "Pont des Soupirs" bridge. This gneiss is representative of the dominant lithology in the Caroux sub-dome; it is

highly deformed and contains a clear foliation and lineation (Figs. 2, 3A). Two samples of Vialais granite (MN 17, MN 19) were collected along the southern boundary of the Espinouse dome, near the contact with the schist of the Rosis syncline and the Caroux sub-dome to the south (Figs. 2, 3B). One sample of undeformed garnet-bearing leucogranite (MN 30) is from the eastern region of the Vialais granite, near the Ourtigas Pass (Figs. 2, 3B). The leucogranite does not exhibit any preferential mineral orientation and clearly crosscuts the other granitoid facies as well as the foliated migmatitic gneiss. Based on field relations, this leucogranite is one of the latest intrusions in the Axial Zone.

5.2. Instrumentation and analytical methods

Monazite, zircon, and xenotime grains were obtained by standard crushing and heavy liquid and isodynamic magnetic separation techniques. The grains were handpicked under ethanol, and only the highest quality, crack-free grains were selected for analysis. U–Th–Pb dating was carried out using two complementary analytical techniques: isotopic dilution thermal ionization mass spectrometry (ID-TIMS) and laser ablation-inductively coupled plasma mass spectrometry (LA-ICPMS).

For ID-TIMS analysis, zircon micro-fractions and single monazite grains were dissolved and analyzed at the University of Clermont-Ferrand (UMR 6524, Magmas et Volcans) following the technique described by Paquette and Pin (2001). Total blanks were 1–10 pg for Pb. The U blanks were negligible. The U and Pb isotopes were analyzed on a Fisons VG Sector 54–30 Mass Spectrometer in multi-collector static mode. Initial common Pb was determined for each fraction using the Stacey and Kramers (1975) two-step model. Analytical uncertainties are listed in Table 1 at 2σ; the individual fraction ellipses were determined using PbDat 1.24 software (Ludwig, 1993).

U–Th–Pb geochronology of zircon, monazite and xenotime was also conducted by LA-ICPMS at the Laboratoire Magmas et Volcans, Clermont-Ferrand (France). Separated zircon, monazite and xenotime grains were mounted in epoxy r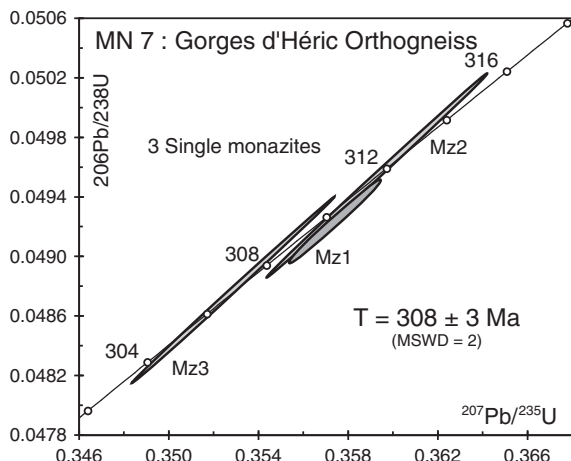esin discs that were polished to reveal equatorial cross sections. Backscatter electron (BSE) and cathodoluminescence (CL) images were used to select points for analysis. The analyses involve the ablation of minerals with a Resonetics Resolution M-50 powered by an ultra short pulse ATL Atlex Excimer laser system operating at a wavelength of 193 nm (detailed description in Müller et al., 2009). For zircon, spot diameters of 26 μm with repetition rates of 4 Hz with laser energy of 5 mJ were used. For monazite and xenotime spot diameters of 7 μm were used, with repetition rates of 1 Hz with a laser energy of 58 mJ. The detailed analytical procedures are described in Hurai et al. (2010) and Roger et al. (2012). GJ-1 zircon standard (Jackson et al., 2004) and Manangotry monazite standard (Horstwood et al., 2003; Paquette and Tiepolo, 2007) were used as an external standard for age calculation. In this study, we used a Manangotry monazite standard to calibrate the Pb/U isotope ratios for xenotime age calculations (see Supplementary material on xenotime U–Pb geochronology using LA-ICPMS and on the choice of analytical standards). Data reduction was carried out with the GLITTER® software package developed by Macquarie Research Ltd (Jackson et al., 2004). The analytical data are provided in Tables 2 and 3 with errors given at ± 1σ.

Ages and diagrams were generated using the Isoplot/Ex v. 2.49 software package by Ludwig (2001). In the text and figures, all uncertainties in ages are given at the 95% confidence level. The decay constants used for the U–Pb system are those determined by Jaffey et al. (1971) and recommended by IUGS (Steiger and Jäger, 1977).

The discordant data analyzed by the LA-ICPMS method were considered only if they allowed possible discordia lines to be defined on the concordia diagrams; otherwise they were not taken into consideration because of doubtful interpretation. In laser-ablation ICPMS analyses, several factors that cannot be easily detected from the inspection of the time-resolved signals might contribute to discordance (e.g. common Pb by way of low U content inclusions, mixing of different age domains, small cracks). Monazite data by LA-ICPMS were plotted in a U–Th–Pb concordia diagram ($^{206}Pb/^{238}U$ vs $^{208}Pb/^{232}Th$) because ^{232}Th measurement is more accurate than ^{235}U.

5.3. Zircon geochronology results

U–Pb and U–Th–Pb analyses on zircon were carried out on samples MN17 and MN19. Zircon from leucogranite sample MN30 was not analyzed because of the high degree of metamictization in the grains. Zircon

Table 1
Analytical results of ID-TIMS U–Pb dating.

Samples[a]	Weight (mg)	Concentrations (ppm)		$^{206}Pb/^{204}Pb$ measured	Atomic ratios[b]			Apparent ages (Ma)[b]		
		U	Pb*		$^{206}Pb^*/^{238}U$	$^{207}Pb^*/^{235}U$	$^{207}Pb^*/^{206}Pb^*$	$^{206}Pb^*/^{238}U$	$^{207}Pb^*/^{235}U$	$^{207}Pb^*/^{206}Pb^*$
Vialais granite										
MN 17: Bardou										
Z 1: Needle, Ab, S, 8 gr	0.005	2365	148	2080	0.0646 ± 0.36	0.495 ± 0.63	0.0556 ± 0.50	404	408	434 ± 11
Z 2: Needle. Ab, S, 7 gr	0.003	2299	136	750	0.0621 ± 0.58	0.479 ± 1.10	0.0559 ± 0.87	389	397	450 ± 19
Z 3: Flat, S-M, 5 gr	0.001	3331	191	187	0.0611 ± 1.10	0.475 ± 2.20	0.0564 ± 1.80	382	394	467 ± 41
MZ 1: Eu, Y, 1 gr	0.002	80357	8535	3074	0.0495 ± 0.28	0.358 ± 0.30	0.0524 ± 0.13	311	310	304 ± 3
MZ 2: Eu, Y, 1 gr	0.002	30047	3263	1032	0.0448 ± 0.21	0.324 ± 0.26	0.0525 ± 0.15	282	285	307 ± 3
MZ 3: Eu, Y, 1 gr	0.001	79899	7737	4035	0.0450 ± 0.25	0.325 ± 0.27	0.0523 ± 0.11	284	286	299 ± 3
MN 19: Douch										
Zr 1: Needle. Ab. M. 10 gr	0.009	1556	75	175	0.0509 ± 0.38	0.390 ± 0.67	0.0556 ± 0.54	320	334	436 ± 12
Zr 2: all. Ab, M. 8 gr	0.008	2257	100	167	0.0509 ± 0.28	0.391 ± 0.53	0.0556 ± 0.43	320	335	438 ± 10
MZ 1: Eu, Y, 1 gr	0.004	6430	2256	475	0.0479 ± 0.32	0.348 ± 0.44	0.0527 ± 0.30	302	303	318 ± 3
MZ 2: Eu, Y, 1 gr	0.002	8236	2763	210	0.0444 ± 0.33	0.325 ± 1.35	0.5311 ± 1.24	280	286	333 ± 14
MZ 3: Eu, Y, 1 gr	0.002	4946	1446	790	0.0445 ± 0.47	0.324 ± 0.88	0.5280 ± 0.72	280	285	320 ± 16
Augen orthogneiss										
MN 07: Gorges d'Héric										
MZ 1: Xeno, Y, 1 gr	0.012	9246	1160	1577	0.0492 ± 0.47	0.357 ± 0.47	0.0526 ± 0.07	310	310	314 ± 2
MZ 2: Xeno, Y, 1 gr	0.045	9532	1073	24152	0.0495 ± 0.62	0.359 ± 0.62	0.0526 ± 0.03	312	312	311 ± 1
MZ 3: Xeno, Y, 1 gr	0.027	11842	1878	25680	0.0488 ± 1.05	0.353 ± 1.05	0.0525 ± 0.04	307	307	306 ± 1

[a] Z: zircon; Mz: monazite; Ab: Abraded; Eu: euhedral; lpr: long prism; spr: short prism; ndl: needle; Trp: transparent; clrls: colorless; Small: grains 50–100 μm in length; Medium: 100–150 μm in length; Large: >150 mm in length.

[b] Isotopic ratios are corrected for mass discrimination (0.1%/amu for Pb and U), isotopic tracer contribution and blanks (1–6 pg for Pb and 1 pg for U) and initial common Pb (Stacey and Kramers, 1975). The errors on the isotopic ratios are quoted in %.

* :radiogenic

Table 2
Analytical results of LA-ICPMS U–Pb dating.

Spot		Concentration (ppm)			Raw ratios								Apparent ages (Ma)								Comment
		Th	U	Th/U	$^{207}Pb/^{206}Pb$	±1σ	$^{206}Pb/^{238}U$	±1σ	$^{2207}Pb/^{235}U$	±1σ	$^{208}Pb/^{232}Th$	±1σ	$^{208}Pb/^{232}Th$	±1σ	$^{207}Pb/^{206}Pb$	±1σ	$^{206}Pb/^{238}U$	±1σ	$^{207}Pb/^{235}U$	±1σ	
MN 17																					
7	Z 1-C	117	418	0.28	0.0564	0.0007	0.0767	0.0009	0.597	0.008	0.0233	0.0003	464.8	5.4	469.3	26.1	476.7	5.2	475.6	4.8	
8	Z 10-C	154	300	0.51	0.0562	0.0007	0.0726	0.0008	0.562	0.008	0.0217	0.0002	434.2	5.0	459.7	28.2	451.6	5	453.1	4.9	
9	Z 14-C	48	247	0.20	0.0573	0.0007	0.0762	0.0009	0.603	0.008	0.0237	0.0003	473.7	6.5	503.1	28.6	473.7	5.2	478.8	5.2	
10	Z 17-C	68	217	0.31	0.0567	0.0007	0.0764	0.0009	0.598	0.008	0.0244	0.0003	488	6.0	479.7	28.6	474.8	5.2	475.8	5.2	
11	Z 22-C	191	364	0.52	0.0602	0.0007	0.0771	0.0009	0.640	0.008	0.0239	0.0003	477.4	5.5	610.5	26.8	479.1	5.2	502.5	5.2	Discordant
12	Z 23-C	88	269	0.33	0.0568	0.0008	0.0765	0.0009	0.599	0.009	0.0225	0.0003	450.1	5.9	483.3	30.4	475.3	5.3	476.8	5.4	
13	Z 24-C	115	195	0.59	0.0554	0.0008	0.0766	0.0009	0.585	0.008	0.0224	0.0003	446.9	5.4	428.2	30.5	475.8	5.3	467.7	5.4	
16	Z 47-C	318	150	2.12	0.1577	0.0017	0.4386	0.0050	9.540	0.114	0.1180	0.0013	2254.6	23.2	2431.5	18.6	2344.4	22.2	2391.4	11	Core
17	Z 47-R	33	314	0.11	0.0562	0.0007	0.0751	0.0009	0.582	0.008	0.0228	0.0004	456	7.1	460	28.4	466.8	5.1	465.8	5.1	
18	Z 48-C	255	213	1.20	0.0709	0.0008	0.1619	0.0018	1.582	0.020	0.0477	0.0005	942.3	10.3	954.3	24.1	967.1	10.2	963.3	7.9	Core
19	Z 48-R	60	850	0.07	0.0562	0.0007	0.0711	0.0008	0.551	0.007	0.0228	0.0003	454.8	6.3	459.7	26.2	443	4.8	445.8	4.6	
20	Z 49-C	431	208	2.07	0.0607	0.0009	0.0940	0.0011	0.787	0.012	0.0281	0.0003	561.1	6.4	628.4	31.2	579.1	6.4	589.2	6.8	Core
21	Z 49-R	42	592	0.07	0.0608	0.0008	0.0783	0.0009	0.657	0.009	0.0421	0.0007	834.3	12.7	632.2	28	486.2	5.4	512.6	5.6	Discordant
22	Z 50-R	296	775	0.38	0.0598	0.0008	0.0664	0.0008	0.548	0.008	0.0208	0.0003	416.2	5.2	598.1	28.3	414.6	4.6	443.8	5	Discordant
24	Z 50-C	966	678	1.42	0.1120	0.0013	0.2546	0.0029	3.931	0.048	0.1384	0.0016	2619.6	27.7	1831.6	20.3	1462.2	14.8	1620.1	9.9	Core
27	Z 61-C	107	227	0.47	0.0595	0.0008	0.0811	0.0009	0.665	0.010	0.0297	0.0004	591	7.4	585.6	29.4	502.6	5.6	517.9	5.8	Discordant
29	Z 61-R	33	674	0.05	0.0585	0.0008	0.0607	0.0007	0.490	0.007	0.0377	0.0007	747.4	13.9	549.4	31.2	380.2	4.3	405.1	5	Discordant
30	Z 62-C	110	329	0.33	0.0634	0.0008	0.1069	0.0012	0.935	0.013	0.0446	0.0006	881.4	10.8	721.9	26.9	655	7.1	670.2	6.6	Core
31	Z 62-R	75	935	0.08	0.0619	0.0008	0.0588	0.0007	0.502	0.007	0.0330	0.0004	656.8	8.9	670.8	26.8	368.2	4.1	412.8	4.5	Discordant
32	Z 6-C	76	170	0.45	0.0562	0.0008	0.0759	0.0009	0.588	0.009	0.0229	0.0003	458.4	6.1	459.1	31.8	471.8	5.3	469.8	5.6	
33	Z 7-C	97	341	0.28	0.0571	0.0008	0.0772	0.0009	0.608	0.009	0.0232	0.0003	462.9	6.2	494.2	29.5	479.3	5.3	482	5.4	
34	Z 16-C	207	357	0.58	0.0564	0.0010	0.0779	0.0009	0.606	0.011	0.0217	0.0003	433.8	6.4	466.5	38.2	483.9	5.6	481	6.7	
MN 19																					
5	Z 1-R	207	551	0.38	0.0630	0.0011	0.0624	0.0006	0.542	0.009	0.0307	0.0006	709.1	38.3	390.1	3.8	439.8	6.2	612.2	12.2	Discordant
6	Z 1-R2	460	826	0.56	0.0557	0.0008	0.0615	0.0006	0.473	0.007	0.0211	0.0004	441.8	32.7	385	3.6	393.3	4.7	422	7.6	
7	Z 3-C	422	431	0.98	0.0513	0.0009	0.0408	0.0004	0.289	0.005	0.0128	0.0002	255.2	39.6	257.8	2.5	257.6	3.8	256.8	4.7	
8	Z 3-R	499	581	0.86	0.0526	0.0008	0.0441	0.0004	0.320	0.005	0.0139	0.0002	310.5	33.4	278.5	2.6	282	3.5	279	5	
9	Z 3-R2	814	820	0.99	0.0592	0.0011	0.0386	0.0004	0.316	0.006	0.0135	0.0003	576	39.2	244.4	2.4	278.6	4.3	271	5	Discordant
11	Z 5-R	253	306	0.83	0.0545	0.0013	0.0488	0.0005	0.367	0.009	0.0132	0.0003	391	52.9	307.1	3.2	317.1	6.3	264.3	6	
15	Z 18-C	716	672	1.07	0.0585	0.0009	0.0632	0.0006	0.510	0.007	0.0200	0.0004	548.5	32.9	394.9	3.7	418.2	5	400.1	7.7	Discordant
16	Z 18-R	140	390	0.36	0.0574	0.0009	0.0686	0.0007	0.542	0.008	0.0221	0.0005	505.4	34,0	427.5	4	440.1	5.4	442.6	9.6	
17	Z 19-C	571	702	0.81	0.0568	0.0010	0.0543	0.0005	0.425	0.007	0.0178	0.0004	482.9	37.6	340.6	3.3	359.6	4.9	357.5	7.4	Discordant
18	Z 24-C	117	326	0.36	0.0522	0.0014	0.0378	0.0004	0.272	0.007	0.0124	0.0004	293.7	62.2	239.5	2.5	244.6	5.9	249.9	7.6	
19	Z 16-C	341	594	0.57	0.0567	0.0008	0.0648	0.0006	0.507	0.007	0.0206	0.0004	479.7	32.3	404.7	3.8	416.2	4.8	412.4	8.6	
20	Z 17-C	368	389	0.95	0.0558	0.0009	0.0665	0.0006	0.512	0.008	0.0201	0.0004	443.2	34.2	415.2	3.9	419.6	5.2	402.1	8.5	
21	Z 17-R	140	234	0.60	0.0550	0.0009	0.0690	0.0007	0.523	0.008	0.0219	0.0005	410.8	36.3	430.2	4	427.2	5.5	438.3	9.8	
22	Z 28-C	380	298	1.27	0.0560	0.0009	0.0674	0.0006	0.521	0.008	0.0207	0.0004	452.1	33.7	420.6	3.9	425.6	5.1	414.4	8.9	Core
23	Z 28-R	60	446	0.13	0.0539	0.0011	0.0533	0.0005	0.396	0.008	0.0183	0.0006	366.2	47.1	335	3.3	339.1	5.9	365.9	12.9	
26	Z 42-C	180	346	0.52	0.0557	0.0009	0.0669	0.0006	0.515	0.008	0.0226	0.0006	441.9	36.8	417.7	4	421.6	5.6	452.4	11	
27	Z 42-R	99	1172	0.08	0.0574	0.0011	0.0526	0.0005	0.417	0.008	0.0226	0.0008	508.3	41.1	330.7	3.2	353.9	5.4	452	15.6	Discordant
28	Z 51-C	202	438	0.46	0.0524	0.0008	0.0482	0.0005	0.349	0.005	0.0150	0.0004	303.1	34.7	303.7	2.8	303.7	3.9	301.2	7.5	
29	Z 51-R	202	387	0.52	0.0523	0.0008	0.0463	0.0004	0.334	0.005	0.0148	0.0004	298.8	36.8	291.5	2.8	292.4	4	297.4	7.6	
30	Z 38-C	45	288	0.16	0.0523	0.0010	0.0432	0.0004	0.311	0.006	0.0167	0.0006	296.9	44.1	272.5	2.6	275.1	4.6	334.9	11.1	
31	Z 38-R	169	179	0.94	0.0530	0.0012	0.0440	0.0004	0.322	0.007	0.0142	0.0004	328.6	49.7	277.9	2.7	283.4	5.3	285	7.7	
32	Z 39-R	64	791	0.08	0.0558	0.0010	0.0479	0.0005	0.369	0.007	0.0163	0.0006	444.8	40.5	301.6	2.9	318.6	4.9	327.9	12.8	
33	Z 39-C	69	358	0.19	0.0580	0.0009	0.0612	0.0006	0.489	0.008	0.0223	0.0007	528	35.7	382.9	3.6	404.3	5.2	446.7	13.1	Discordant

Z or Zr: zircon.
R: rim and C: center.

Table 3
Analytical results of LA-ICPMS U–Pb dating.

Spot		Ratios								Ages (Ma)							
		$^{207}Pb/^{206}Pb$	$\pm 1\sigma$	$^{206}Pb/^{238}U$	$\pm 1\sigma$	$^{207}Pb/^{235}U$	$\pm 1\sigma$	$^{208}Pb/^{232}Th$	$\pm 1\sigma$	$^{207}Pb/^{206}Pb$	$\pm 1\sigma$	$^{206}Pb/^{238}U$	$\pm 1\sigma$	$^{207}Pb/^{235}U$	$\pm 1\sigma$	$^{208}Pb/^{232}Th$	$\pm 1\sigma$
MN 17																	
7	MZ 1	0.0517	0.0007	0.0494	0.0006	0.352	0.005	0.0155	0.0002	271.1	30.2	311.2	3.7	306.4	3.8	311	3
8	MZ 2	0.0509	0.0007	0.0480	0.0006	0.337	0.005	0.0151	0.0002	236.2	30.7	302.4	3.6	294.9	3.7	303	3
9	MZ 3	0.0515	0.0007	0.0487	0.0006	0.346	0.005	0.0150	0.0002	264.3	30.5	306.5	3.6	301.6	3.8	302	3
10	MZ 4	0.0500	0.0007	0.0486	0.0006	0.335	0.005	0.0151	0.0002	196.3	32	305.9	3.6	293.5	3.8	303	3
11	MZ 5	0.0506	0.0007	0.0478	0.0006	0.334	0.005	0.0153	0.0002	223.2	30.2	301.2	3.5	292.4	3.7	308	3
12	MZ 7	0.0506	0.0007	0.0478	0.0006	0.333	0.005	0.0152	0.0002	223	31.4	300.9	3.5	292.1	3.8	304	3
13	MZ 8	0.0504	0.0007	0.0481	0.0006	0.334	0.005	0.0152	0.0002	211.4	31.4	303	3.6	292.6	3.8	305	3
14	MZ 9	0.0503	0.0007	0.0485	0.0006	0.337	0.005	0.0152	0.0002	211.2	32.3	305.6	3.6	294.9	3.9	305	3
17	MZ 10	0.0504	0.0007	0.0469	0.0006	0.325	0.005	0.0152	0.0002	211.9	31	295.3	3.5	286.1	3.6	306	3
18	MZ 13	0.0495	0.0007	0.0486	0.0006	0.332	0.005	0.0152	0.0002	169.8	33.5	306.2	3.6	290.9	3.9	304	3
19	MZ 27	0.0505	0.0007	0.0469	0.0006	0.327	0.005	0.0150	0.0002	219.5	33.2	295.5	3.5	287.1	3.9	301	3
20	MZ 26	0.0509	0.0007	0.0473	0.0006	0.332	0.005	0.0150	0.0002	236.9	33.2	298.1	3.5	291.2	3.9	300	3
21	MZ 25	0.0501	0.0008	0.0489	0.0006	0.338	0.005	0.0150	0.0002	198.9	35.2	307.9	3.6	295.5	4.2	301	3
22	MZ 24	0.0499	0.0008	0.0489	0.0006	0.336	0.005	0.0151	0.0002	189.8	35.6	307.5	3.6	294.1	4.2	303	3
23	MZ 20	0.0512	0.0008	0.0483	0.0006	0.340	0.005	0.0152	0.0002	248.3	34.4	303.8	3.6	297.5	4.1	306	3
24	MZ 18	0.0509	0.0008	0.0475	0.0006	0.333	0.005	0.0151	0.0002	235.5	35	299	3.5	291.9	4.1	304	3
MN 19																	
7	MZ 1	0.0538	0.0013	0.0488	0.0006	0.362	0.009	0.0150	0.0002	364.5	54.5	307	3.8	313.8	6.7	300	3
8	MZ 2	0.0499	0.0007	0.0491	0.0006	0.337	0.005	0.0152	0.0002	189.1	32.9	308.9	3.6	295.3	3.9	305	3
9	MZ 3	0.0508	0.0007	0.0485	0.0006	0.340	0.005	0.0150	0.0002	234	32.7	305.6	3.6	297.4	4	302	3
10	MZ 4	0.0498	0.0007	0.0472	0.0006	0.324	0.005	0.0151	0.0002	185.6	30.8	297.6	3.5	285.3	3.6	302	3
11	MZ 5	0.0505	0.0007	0.0471	0.0006	0.328	0.005	0.0152	0.0002	219.6	31.7	296.8	3.5	288.2	3.7	304	3
12	MZ 6	0.0507	0.0007	0.0487	0.0006	0.340	0.005	0.0151	0.0002	225.5	33.2	306.3	3.6	297.1	4	302	3
13	MZ 9-1	0.0506	0.0008	0.0503	0.0006	0.351	0.006	0.0150	0.0002	222.5	37.3	316.3	3.7	305.3	4.5	230	3
14	MZ 9-2	0.0503	0.0007	0.0483	0.0006	0.335	0.005	0.0152	0.0002	209	34	303.8	3.6	293.1	4	304	3
17	MZ 22	0.0581	0.0021	0.0486	0.0006	0.390	0.014	0.0150	0.0002	534.7	76.2	306	4	334.1	10.1	301	3
19	MZ 13	0.0512	0.0008	0.0471	0.0006	0.333	0.005	0.0151	0.0002	250	34.9	297	3.5	291.7	4.1	303	3
20	MZ 23	0.0509	0.0009	0.0474	0.0006	0.333	0.006	0.0146	0.0002	238.4	38.4	298.5	3.5	291.7	4.4	293	3
21	MZ 24	0.0509	0.0009	0.0479	0.0006	0.336	0.006	0.0150	0.0002	236	40.7	301.9	3.6	294.5	4.7	300	3
22	MZ 15	0.0505	0.0008	0.0459	0.0006	0.320	0.005	0.0151	0.0002	219.4	36.4	289.5	3.4	281.9	4.1	304	3
23	MZ 16	0.0512	0.0008	0.0467	0.0006	0.329	0.006	0.0147	0.0002	248.3	37	294	3.5	288.9	4.3	296	3
24	MZ 27	0.0507	0.0008	0.0480	0.0006	0.336	0.006	0.0149	0.0002	228.8	38.1	302.5	3.6	294.1	4.4	299	3
MN 30																	
8	MZ 1	0.0506	0.0006	0.0476	0.0006	0.332	0.004	0.0153	0.0002	222.1	27.3	299.5	3.4	290.9	3.3	307	3
9	MZ 2	0.0503	0.0006	0.0467	0.0005	0.324	0.004	0.0148	0.0002	207.7	27.7	294.3	3.4	284.8	3.3	298	3
10	MZ 3	0.0504	0.0006	0.0464	0.0005	0.322	0.004	0.0150	0.0002	213.5	27.9	292.4	3.4	283.8	3.3	300	3
11	MZ 6-1	0.0502	0.0006	0.0472	0.0005	0.327	0.004	0.0151	0.0002	205.3	27.9	297.5	3.4	287.3	3.3	304	3
12	MZ 6-2	0.0561	0.0007	0.0469	0.0005	0.363	0.005	0.0149	0.0002	456.3	26.4	295.4	3.4	314.3	3.6	300	3
13	MZ 9-1	0.0503	0.0006	0.0459	0.0005	0.319	0.004	0.0152	0.0002	209.7	28.3	289.4	3.3	280.8	3.3	305	3
14	MZ 9-2	0.0503	0.0006	0.0474	0.0006	0.329	0.004	0.0152	0.0002	210.2	28.7	298.3	3.4	288.5	3.4	305	3
15	MZ 13	0.0504	0.0006	0.0470	0.0005	0.327	0.004	0.0149	0.0002	213.8	28.4	296.3	3.4	287.2	3.4	298	3
18	XE 2	0.0506	0.0006	0.0476	0.0006	0.333	0.005	0.0159	0.0002	224.4	28.9	300.1	3.4	291.6	3.5	319	4
21	XE 13	0.0501	0.0006	0.0479	0.0006	0.331	0.005	0.0160	0.0002	200.5	29.7	301.9	3.5	290.5	3.5	320	4
22	XE 10	0.0499	0.0006	0.0474	0.0006	0.327	0.005	0.0155	0.0002	192.5	30.2	298.8	3.4	287	3.5	310	4
23	XE 9	0.0503	0.0007	0.0465	0.0005	0.322	0.005	0.0158	0.0002	209	30.3	293	3.4	283.8	3.5	316	4
24	XE 12	0.0502	0.0007	0.0468	0.0005	0.327	0.005	0.0159	0.0002	202.3	30.6	295.1	3.4	284.9	3.5	318	4
25	XE 16	0.0505	0.0007	0.0477	0.0006	0.332	0.005	0.0158	0.0002	216.1	30.7	300.3	3.5	290.9	3.6	316	4
28	XE 17	0.0503	0.0007	0.0475	0.0006	0.329	0.005	0.0157	0.0002	207.2	31.6	299.4	3.4	289.1	3.7	315	4
30	XE 11	0.0498	0.0007	0.0470	0.0006	0.322	0.005	0.0155	0.0002	184.8	32.4	296	3.4	283.8	3.7	312	4
31	XE 1	0.0504	0.0007	0.0475	0.0006	0.330	0.005	0.0157	0.0002	212.3	32.5	299.4	3.5	289.7	3.8	316	4
32	MZ 4	0.0495	0.0007	0.0473	0.0006	0.323	0.005	0.0150	0.0002	172.7	33	298	3.4	284.2	3.7	302	3
33	MZ 5	0.0503	0.0007	0.0467	0.0005	0.324	0.005	0.0151	0.0002	209.6	33.7	294	3.4	284.8	3.8	303	3
34	MZ 7	0.0500	0.0007	0.0470	0.0006	0.324	0.005	0.0151	0.0002	196.3	33.8	296.1	3.4	285.1	3.8	302	3

Mz: monazite, X: xenotime.

ages from the Héric augen gneiss (sample MN7) were reported in Roger et al. (2004) (see previous geochronology Section 4 and Fig. 5B).

Most of the analyzed zircons from samples MN17 and MN19 are euhedral, transparent, and colorless. CL images show that most zircons have complex internal structures (sector zoning and inherited cores) (Fig. 4A, B). Well-preserved euhedral growth zones with unperturbed oscillatory zoning are also present. This zoning is characteristic of zircon crystallized from magma (Hanchar and Miller, 1993; Hoskin, 2000). Magmatic zoning develops either in continuity with euhedral cores or surrounding resorbed rounded cores. Non-magmatic zircon (i.e. metamorphic, recrystallized, or hydrothermal) tends to have poorly-defined internal zoning with, in some instances, non-geometric patchy zoning (Pidgeon, 1992; Hanchar and Miller, 1993; Hoskin and Black, 2000). Commonly, igneous zircon grains have characteristically higher Th/U ratios (>0.1) that do not overlap with Th/U ratios of non-igneous zircon (<0.1) (Williams and Claesson, 1987; Vavra et al., 1996; Hoskin and Black, 2000; Hartmann and Santas, 2004).

For ID-TIMS dating, crystals that are small (80–150 μm in length), needle-shaped or flat diamond-shaped were selected because they rarely show inherited cores. Prior to dissolution, zircons were mechanically abraded (Krogh, 1982) except one fraction of small flat-shaped crystals (Table 1).

Table 4
Compilation of Variscan U–Th–Pb ages. (*: *recalculated age* (see detail in the text))

No.	Locality	Sample	Age (±2σ)	Mineral	Technique	References
1	Gorges d'Héric	Orthogneiss (MN 7)	308 ± 3 Ma	Mz	TIMS	This study
2	Vialais (Bardou)	Deformed granite (MN17)	303 ± 10 Ma	Mz	TIMS	
			304 ± 2 Ma	Mz	LA-ICPMS	
3	Vialais (Douch)	Deformed granite (MN 19)	315 ± 11 Ma	Mz	TIMS	
			301 ± 2 Ma	Mz	LA-ICPMS	
4	Ourtigas	Undeformed Gt-granite (MN 30)	299 ± 4 Ma	Mz	LA-ICPMS	
			298 ± 2 Ma	Xe	LA-ICPMS	
5	Héric	Syn-tectonic Meta-aplitic dyke (Heric 6)	309 ± 3 Ma	Z	TIMS	Franke et al. (2011)
			313 ± 1 Ma	Mz	TIMS	
6	Ste Eutrope	Orthogneiss (structure S/C)	294.4 ± 4 Ma	Mz	LA-ICPMS	Pitra et al. (2012)
7	Montalet	Deformed syn-kinematic Gt-granite (S/C structure) (ES 5)	294 ± 1 Ma	Mz	LA-ICPMS	Poilvet et al. (2011)
			294 ± 3 Ma	Z	LA-ICPMS	
8	Montalet	Gt-granite	327 ± 7 Ma	Mz	EPMA	Faure et al. (2010)
			324 ± 3 Ma	Z	SIMS	
			305 ± 10 Ma*	Z	SIMS (recalculated age)	
9	La Salvetat	Migmatite	305 ± 6 Ma	Z	SIMS	
10	Laouzas	Undeformed granite	299 ± 8 Ma	Z	SIMS	
			333 ± 6 Ma	Mz	EPMA	
11	Soulié	Undeformed granite	318 ± 4 Ma	Mz	EPMA	
12	Vialais	Undeformed granite	320 ± 3 Ma	Mz	EPMA	
13	Vialais	Deformed granite (magmatic foliation)	327 ± 3 Ma	Mz + Z	TIMS	Matte et al. (1998)
14	Peyrambert farm	Eclogite	314 ± 2.5 Ma	Z	SHRIMP II	Faure et al. (2014)
			311 ± 2 Ma	Z	SIMS	
			308 ± 4 Ma	R	SIMS	

5.3.1. Sample MN17 (Vialais granite)

Two needle-type and one flat-type zircon fractions (with 5 to 8 grains each) were analyzed with ID-TIMS. The U content ranges from 3331 ppm to 2299 ppm; Pb content varies from 191 ppm to 136 ppm (Table 1). In the concordia diagram, ages are discordant and the weighted average ^{207}Pb/^{206}Pb age is 439 ± 29 Ma (MSWD = 2) (Fig. 5A). With LA-ICPMS, 22 analyses were carried out on 16 grains (Table 2, Fig. 6A). CL images show that most zircon grains have complex internal structures (Fig. 4A); 16 grains show magmatic growth zoning with a U content ranging from 150 to 678 ppm and Th/U ratios from 0.2 to 2.2 in the core of the crystals. Among these cores, five spots (#16, 18, 20, 24, 30) indicate inherited ^{207}Pb/^{206}Pb age components of 2.4 Ga, 1.8 Ga, 0.9–1 Ga and 0.7–0.6 Ga. Their Th/U ratio range from 1.20 to 2.12 (except spot #30: Th/U = 0.335); all these features suggest multiple magmatic sources for the protolith. Rims and cores of six zircon grains (Zr 47, 48, 49, 50, 61, 62) have been investigated; all rims (spots #17, 19, 21, 22, 29, 31) are characterized by a U concentration ranging from 314 to 935 ppm, and a low Th/U ratio ranging from 0.05 to 0.1 (except spot #22, with Th/U = 0.38) that would indicate a possible metamorphic origin for the grains. Spots #17 and 19 are concordant and sub-concordant and yield ^{206}Pb/^{238}U ages of 466.8 ± 10.3 Ma and 443 ± 9.7 Ma (±2σ), respectively, with a ^{207}Pb/^{206}Pb age around 460 Ma (Table 2, Fig. 6A). Nine analyses (#7, 9, 10, 12, 13, 17-rim, 32, 33, 34) form a concordant cluster yielding a concordia age of 474.9 ± 3.4 Ma (MSWD = 0.1). These points have U concentrations between 170 and 418 ppm. Their Th/U ratio ranges from 0.20 to 0.59 (except for spot #17), a typical ratio for an igneous zircon origin. Some points are discordant within the concordia diagram (points 11, 27 are core data, and 21, 22, 29, 31 are rim data), indicating that the U–Pb system was disturbed, but no Variscan ages were measured in the zircon grains from this sample.

5.3.2. Sample MN19 (Vialais granite)

Two fractions of eight and 10 grains of abraded zircon were analyzed with ID-TIMS (Table 1, Fig. 4). Both ages are similar and very discordant. The weighted average ^{207}Pb/^{206}Pb age is 437 ± 8 Ma (MSWD = 0.04) (Fig. 5A). This age is obtained on only two points, but it is consistent with the age from sample MN17. The linear regression through the five analytical points of these two Vialais granite samples yields an upper intercept of 439 ± 10 Ma and a lower intercept of −3 ± 49 Ma

(MSWD = 1.4) (Fig. 5A). In the concordia diagram, the analytical points are in discordant positions, and the age of 439 ± 10 Ma must be interpreted as a minimum age of the magmatic protolith emplacement.

Using LA-ICP-MS, 23 spots on both cores and rims of 13 zircon grains were analyzed (Table 2). In the concordia diagram, the discordant ages (spots #9, 27, 17, 33, 5, 15) were not taken into consideration in the discussion and the interpretation (Fig. 6B). Seventeen spots are in concordant or sub-concordant positions, and the ^{207}Pb/^{206}Pb ages vary between 240 and 440 Ma (Table 2, Fig. 6B). The histogram of the concordant or sub-concordant ^{207}Pb/^{206}Pb ages clearly reveals two distinct populations, one around 440 Ma and another around 300–310 Ma (Fig. 6C). The weighted average ^{207}Pb/^{206}Pb ages of the oldest and youngest populations are 455 ± 25 Ma (MSWD = 0.8) and 298 ± 29 Ma (MSWD = 0.3), respectively (Fig. 6D). Five analyses (#16, 20, 21, 22, 26) form a concordant cluster yielding a concordia age of 422.7 ± 6.4 Ma (2σ; MSWD = 6.2) (Fig. 6B). For the youngest population, spots #28, 11, 32, 29, 31, 8, 30, 7, 18 plot in concordant position between 300 and 240 Ma. This relatively wide age range is probably related to radiogenic Pb loss in the younger crystals. Analysis #23 yields an isolated concordant age of 335 ± 6.6 Ma that probably corresponds to a mixed age between an old core (spot #22) with an age of 422 Ma and a younger rim with a probable Variscan age (300–310 Ma). The Th/U ratio ranges between 0.36 and 1.27 for the oldest zircons and between 0.15 and 0.98 for the youngest zircons (Table 2). In both cases, these values are typical of igneous zircon.

5.4. Monazite and xenotime geochronology results

Monazite grains for the four samples are of moderate size (100–200 μm), transparent and euhedral to subhedral. BSE and CL images show a mostly homogeneous structure without cores and rims (Fig. 4C–E). The monazite crystals for samples MN7, MN17 and MN19 are yellow. The color changes to greenish for grains obtained from leucogranite sample MN30 (Fig. 3B); this sample contains both monazite and xenotime (Fig. 4E, F).

5.4.1. Sample MN7 (Héric augen gneiss)

Three single grains of monazite were analyzed from this sample of augen gneiss from the Gorges d'Héric (Fig. 2). The Pb and U contents are 1073–1878 ppm and 9246–11,842 ppm, respectively (Table 1). In the concordia diagram, the points are concordant to sub-concordant

around 310 Ma. A linear regression of these three points gives an age of 308 ± 3 Ma (MSWD = 2) (Fig. 7). The weighted average of the $^{206}Pb/^{238}U$ and $^{207}Pb/^{235}U$ ages are 310.4 ± 4.3 Ma and 310.1 ± 4.3 Ma, respectively. The age of 308 ± 3 Ma is interpreted as the metamorphic age.

5.4.2. Sample MN17 (Vialais granite)

ID-TIMS analyses show that three single grains of monazite display U and radiogenic Pb concentrations of 3 to 8 wt.% and 3345 to 8612 ppm, respectively (Table 1). The upper intercept age is 302.6 ± 9.9 Ma (MSWD = 7.5) (Fig. 8A). With LA-ICP-MS, 16 spot analyses were carried out on 16 monazite grains. All ellipses are concordant and give a concordia age of 303.6 ± 2 Ma (MSWD = 2.1) with a weighted average $^{206}Pb/^{238}U$ age of 303.0 ± 2.4 Ma (MSWD = 1.6) (Table 3, Fig. 8B).

5.4.3. Sample MN19 (Vialais granite)

Three monazite single grains were analyzed with ID-TIMS (Table 1). The Pb and U contents are 1446 to 2763 ppm and 4946 to 8236 ppm, respectively. The data points are slightly discordant. A linear regression of these points gives an age of 315 ± 11 Ma for the upper intercept and −81 ± 230 Ma for the lower intercept (MSWD = 0.62) (Fig. 8C). The analytical point Mz1 is sub-concordant with a $^{206}Pb/^{238}U$ age of 302 ± 1 Ma and a $^{207}Pb/^{235}U$ age of 303 ± 2 Ma (Table 1).

With LA-ICP-MS, 16 spot analyses were carried out on 14 monazite grains. Two monazite crystals (#9, 22) were analyzed both in the core and near the rim and show similar U/Pb ages, indicating that the grains are homogeneous. Fifteen spots are concordant or sub-concordant yielding a concordia age of 301.2 ± 2.4 Ma (MSWD = 1); this agrees well with the weighted average $^{206}Pb/^{238}U$ age of 300.8 ± 3.3 Ma (MSWD = 2.5, except spot #13) (Table 3, Fig. 8D).

5.4.4. Sample MN30 (Ourtigas leucogranite)

Garnet-bearing leucogranite sample MN30 was dated only by LA-ICPMS (Table 3). Eleven spots on 9 monazite grains were analyzed. In a concordia diagram, the ages are concordant and the concordia age is 298.6 ± 3.5 Ma (Fig. 8E). The weighted average $^{206}Pb/^{238}U$ age is 295 ± 2 Ma (MSWD = 0.75, n = 11) (Fig. 8F).

Xenotime from sample MN30 was also analyzed using LA-ICPMS (see Supplementary material on xenotime U–Pb geochronology using LA-ICPMS and on the choice of analytical standards). On a concordia diagram, the ages from 9 xenotime grains are at a similar position as the monazite ages (Fig. 8E). However, a slight discrepancy could be related to the use of a monazite (and not xenotime) standard (see Supplementary material). The weighted average $^{206}Pb/^{238}U$ age for these data is 298.2 ± 2.2 Ma (MSWD = 0.71, n = 9) (Fig. 8F), in agreement with the weighted average $^{206}Pb/^{238}U$ age of 296.7 ± 1.5 Ma calculated from both xenotime and monazite data (MSWD = 0.85, n = 20) (Fig. 8F).

6. Interpretation of age data

Zircon, monazite, and xenotime U/Pb ages obtained in this study indicate a complex crystallization history for the Montagne Noire gneiss and granite. A majority of Th/U ratios of analyzed zircons (Precambrian to Paleozoic) are consistent with a magmatic origin. Zircons of the Héric augen gneiss (MN7) yielded ages of 450–460 Ma, interpreted as the minimum emplacement age of the granitic protolith (Roger et al., 2004). More recently, Franke et al. (2011) dated the augen gneiss at the same locality; in that study, zircons show an inverse discordia line with a lower intercept at 416 + 4/−6 Ma that is interpreted as the minimum age of crystallization of the granite protolith.

Zircon ages from sample MN17 indicate the presence of the same 475–450 Ma magmatic source dated by both ID-TIMS and LA-ICPMS methods (Figs. 5, 6). This Ordovician event has been interpreted as the emplacement age of the protolith to the Montagne Noire augen gneiss (Cocherie et al., 2005; Faure et al., 2010). Some inherited zircon cores

from the sample collected near Bardou (MN17; Fig. 2), indicate the occurrence of older magmatic sources (2.4 Ga, 1.8 Ga, 1.0–0.9 Ga and 0.7–0.6 Ga) (Fig. 6A). However, this sample does not reveal any late Paleozoic (Variscan) ages. The absence of Variscan ages associated with the concordant position of all the data points on the concordia plot is a strong argument to interpret the 474.9 ± 3.4 Ma magmatic zircon age as an intrusion age for the protolith of the Montagne Noire augen gneiss (Fig. 6A). This age is more accurate than the minimum age of 439 ± 29 Ma obtained by ID-TIMS and defined by only three points that are discordant (Fig. 5A); however, ID-TIMS and LA-ICPMS ages are similar within error.

Results from sample MN19 show that both Th/U ratios and the histogram of concordant zircon grains indicate the occurrence of two distinct populations, both of magmatic origin, around 440–420 Ma and 310–300 Ma (Fig. 6C). The early Paleozoic age group is confirmed by a cluster of concordant points yielding a concordia age of 422.7 ± 6.4 Ma, and by the 437 ± 8 Ma value obtained by ID-TIMS on two zircon fractions (Figs. 5, 6B). Inherited components older than early Paleozoic were not found in this sample. The combined occurrence of early Paleozoic and Late Carboniferous concordant magmatic zircon ages suggests that zircon preserved the information of their early Paleozoic magmatic origin while a new generation of zircon, or rim overgrowths around these early Paleozoic zircons, crystallized from a Late Carboniferous partial melt.

Taken together, the new zircon ages are consistent with previously published work, identify the protolith of the Montagne Noire augen gneiss as an Ordovician granite, and indicate that the gneiss was the likely source of the melt that produced the Vialais granite and other anatectic intrusions. Our new results also document the U–Pb monazite age of the Héric augen gneiss (sample MN7) to be 308 ± 3 Ma, similar to the zircon and monazite ages from a meta-aplite dike at the same locality (309–313 Ma, Franke et al., 2011). Our results also reveal a single population of monazite in the Vialais granite. The monazite U/Pb ages obtained by ID-TIMS and LA-ICPMS methods on both granite samples MN17 and MN19 are the same within error (303.6 ± 2 Ma and 301.2 ± 2.4 Ma). Based on these two samples, the weighted average U/Pb monazite age in the late kinematic Vialais granite is 303 ± 4 Ma (MSWD = 2.4, n = 4) (Fig. 9).

The undeformed garnet-bearing leucogranite sample MN30 collected near Ourtigas (Fig. 2) yielded a monazite concordia age of 298.6 ± 3.5 Ma, in good agreement with the weighted average $^{206}Pb/^{238}U$ age of 298.2 ± 2.2 Ma that was obtained from xenotime (Fig. 8E, F). These ages are interpreted as the age of emplacement of the post-kinematic Ourtigas leucogranite at 298 ± 2 Ma (MSWD = 0.24, n = 2) (Fig. 9).

These new U–Pb monazite ages obtained on augen gneiss, late-kinematic Vialais, and post-kinematic Ourtigas leucogranite bracket the high-temperature deformation and metamorphism in the Montagne Noire at ~315–300 Ma. These results contrast with previous work that reported ages for the Vialais granite of between 330 and 320 Ma (Matte et al., 1998; Faure et al., 2010). Our new ages join a growing body of geochronological evidence for late Variscan high-temperature metamorphism in the Montagne Noire, including SIMS zircon ages of the anatectic Laouzas granite (299 ± 8 Ma) and the Salvetat migmatite (306 ± 6 Ma) from the central part of the Espinouse dome (Faure et al., 2010) (Fig. 1). More recently, U/Pb LA-ICPMS ages of 294 ± 3 Ma (zircon) and 294 ± 1 Ma (monazite) have been reported for the Montalet granite further north in the Espinouse dome (Fig. 1) (Poilvet et al., 2011).

Faure et al. (2010) reported older ages for the Montalet granite; monazite yielded an age of 327 ± 7 Ma by electron microprobe and zircon was dated at 324 ± 3 Ma by SIMS. For this granite, four analytical points are concordant to sub-concordant within the Tera–Wasserburg diagram (Fig. 12 in Faure et al., 2010) and yielded a younger age of ~310–300 Ma. The weighted average $^{206}Pb/^{238}U$ age published by Faure et al. (2010) is 305 ± 10 Ma (MSWD = 0.96). This new age is similar within error to the ages obtained by LA-ICPMS on zircon and
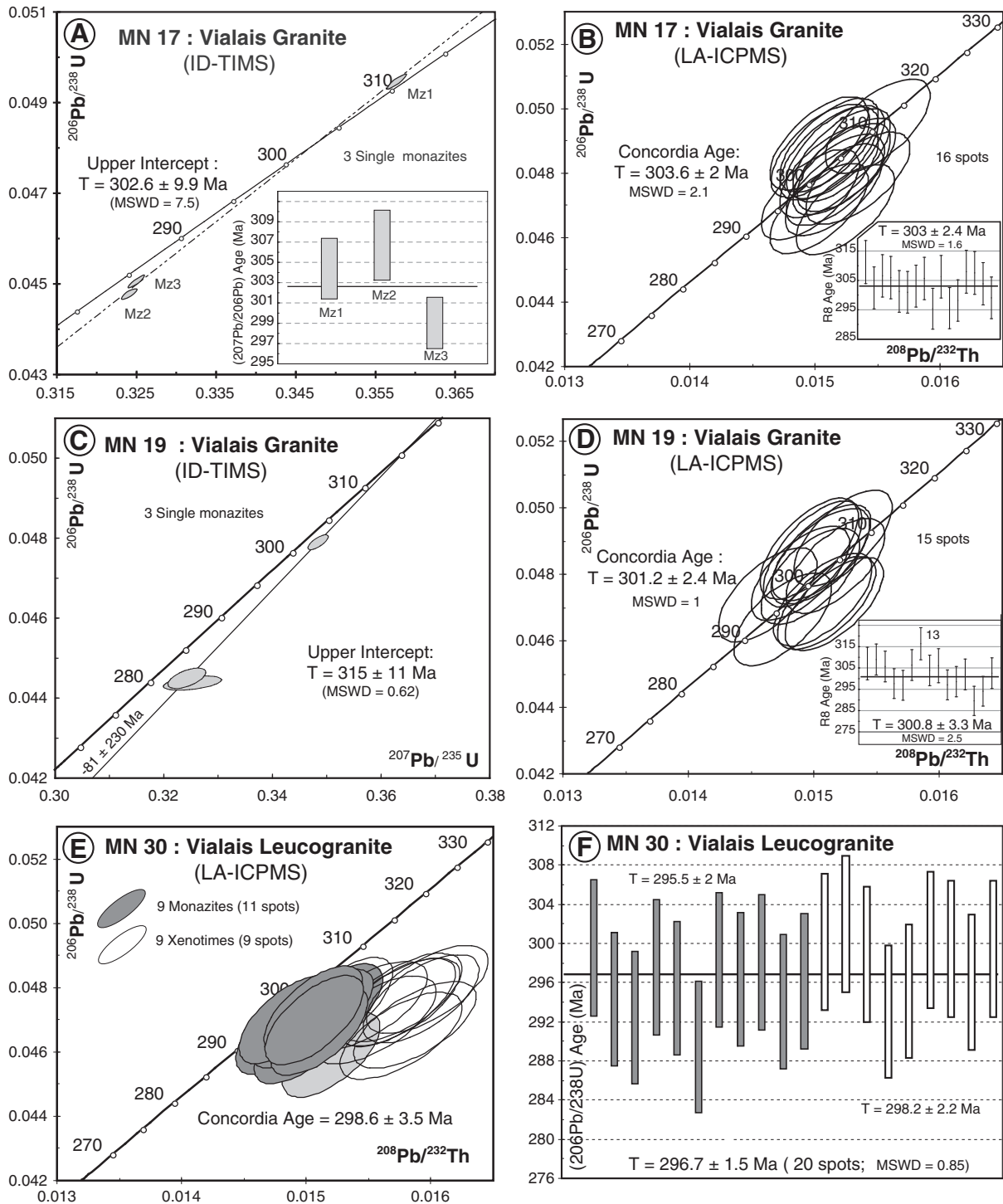
Fig. 8. Monazite and xenotime U–Pb diagrams obtained with ID-TIMS (A and C) or LA-ICPMS (B, D, E and F). A and B) Vialais granite near Bardou (sample MN17). C and D) Vialais granite near Douch (sample MN 19). E and F) Garnet-bearing leucogranite near the Ourtigas Pass (sample MN 30).

monazite by Poilvet et al. (2011). In their interpretation of geochronology data, Faure et al. (2010) did not take into account SIMS zircon ages younger than 318 Ma, invoking Pb loss to explain the young ages of the Montalet and Laouzas granites and La Salvetat migmatite. If we consider that the granite was emplaced at ~300 Ma, the four concordant to sub-concordant points at ~330–320 Ma of Faure et al. (2010) can be interpreted either as inherited cores dated at 324 ± 3 Ma or as a mixing of different age domains (a rim at 300 Ma and a core at 450–460 Ma). In the Tera–Wasserburg diagram of zircons from the La Salvetat migmatite and Laouzas granite (Fig. 12 in Faure et al., 2010), there is no concordant

to sub-concordant point around 330–320 Ma. Finally, all these ages are similar to the ID-TIMS zircon lower intercept age of 309 ± 3 Ma obtained by Franke et al. (2011) for the syn-kinematic aplite dike located on the same outcrop as our sample M7 in the Gorges d'Héric.

K–Ar (Franke et al., 2011) and $^{40}Ar/^{39}Ar$ (Maluski et al., 1991) results for muscovite and biotite revealed a cluster of ages at 300–290 Ma, both in the uppermost gneiss of the Axial Zone and in Paleozoic units along the southern and northern margins of the Axial Zone (Franke et al., 2011). The similarity between K–Ar, $^{40}Ar/^{39}Ar$, and our U–Pb monazite ages implies relatively rapid cooling.
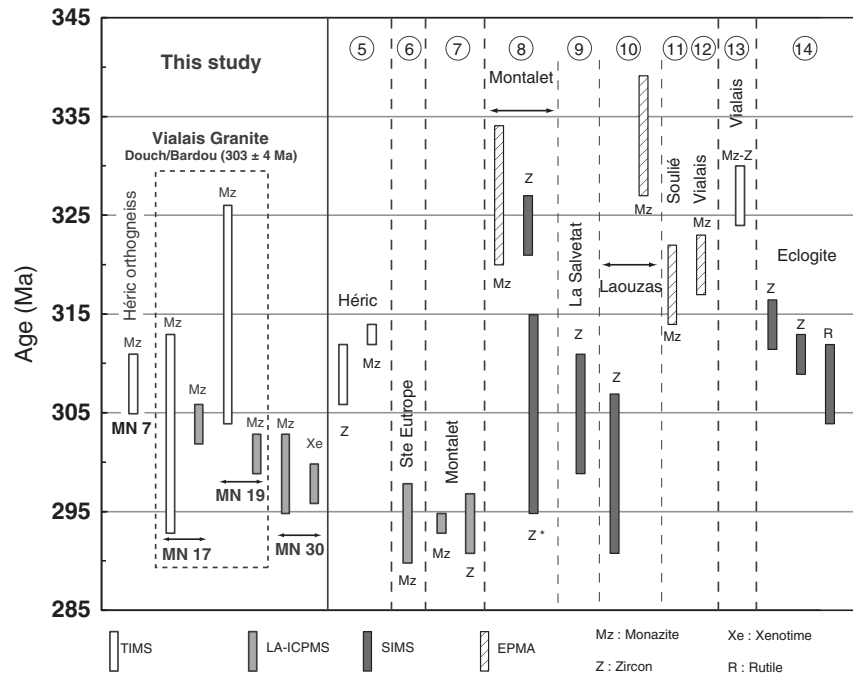
Fig. 9. Synthesis of U–Th–Pb Variscan ages obtained in this study, and compilation of ages from the literature (see detail in the text and Table 4). Uncertainties in ages are ±2σ.

In the eastern Montagne Noire Axial Zone, $^{40}Ar/^{39}Ar$ ages of 297 ± 3 Ma for muscovite are recorded in both the metasedimentary rocks along the basal sole thrust of the Paleozoic nappes and the leucogranite mylonites of the Espinouse detachment shear zone (Fig. 2) (Maluski et al., 1991). These ages document the timing of cooling and synmetamorphic ductile shearing along the main extensional detachments that controlled the evolution of Late Carboniferous basins. These $^{40}Ar/^{39}Ar$ ages agree well, within error, with the 294.4 ± 4 Ma age obtained on monazite (U–Th–Pb, LA-ICPMS) extracted from the sheared Saint-Eutrope orthogneiss on the northern flank of the Espinouse dome (N of the Vialais granite) and interpreted as the age of deformation along the Espinouse detachment (Pitra et al., 2012).

Emplacement of the Vialais granite was synchronous with the development of the Espinouse normal shear zone and the formation of Late Carboniferous (Stephanian) basins in the hanging wall. Deposition of the basin fill started prior to regional volcanic activity that included trachytic and rhyolitic tuffaceous deposits (cinerites) in the Graissessac (Fig. 1) and Roujan-Neffies (to the SE of the Montagne Noire) piedmont basins. U–Th–Pb analysis of zircon from these cinerite formations yielded ages of 295 ± 5 Ma (Graissessac) and 298 ± 5 Ma (Roujan-Neffies) (Bruguier et al., 2003). These authors associated this volcanic event with a phase of extensional tectonics along strike–slip or transtensional corridors.

7. Mechanisms of Montagne Noire dome formation

The origin of doming and the structural relations between the Axial Zone and the southern and northern units of the Montagne Noire have been debated for many decades. Proposed mechanisms for the formation of the dome include diapirism (Gèze, 1949; Schuiling, 1960; Faure and Cottereau, 1988; Faure et al., 2010), contraction forming an E–W trending anticline following nappe stacking (Arthaud, 1970; Mattauer et al., 1996; Matte et al., 1998; Demange, 1999; Matte, 2007), doming associated with a vertical strike–slip shear zone (Nicolas et al., 1977), syn-contraction erosion and exhumation of high-grade rocks during nappe emplacement (Malavieille and Konstantinoskaya, 2010), or oblique extension and development of a

metamorphic core complex during post-thickening orogenic collapse (Echtler and Malavieille, 1990; Van den Driessche and Brun, 1992; Brun and Van den Driessche, 1994, 1996; Franke et al., 2011).

A variation of the core complex model proposes that the formation of the migmatite dome was initiated by upper crustal extension and coeval activation of flow in the low-viscosity crust (Rey et al., 2011a,b). In this model, the flowing crust converges beneath the zone of extension, producing contractional structures and the formation of a vertical high-strain zone in which channel material moves from deeper to shallower crustal levels. This material is then transferred into an extensional detachment system where it is finally exhumed. This model predicts a double dome geometry, synchronous extension in the upper crust and contraction at depth, and a deformation sequence from contraction to extension as rocks are progressively exhumed (Fig. 10A). The final structure of these 2D models has the geometry of a diapir with a central stem and a double dome 'mushroom' geometry; yet Rey et al. (2011a,b) modeling also shows that this structure persists whether buoyancy forces are turned on or off in the model, suggesting that buoyancy enhances ascent but is not the main driver of exhumation of partially molten crust. Application of the Rey et al. (2011a,b) model to the Montagne Noire dome has been controversial (see comment and reply, Van Den Driessche and Pitra, 2012; Rey et al., 2011a,b). Our new data allow a better evaluation of this model in relation to other models for dome formation.

The critical results of our study are as follows:

(1) high-temperature deformation of the augen gneiss, including upright folding and prominent E–W stretching, developed around 308 ± 3 Ma;

(2) crystallization of the Vialais granite at 303 ± 4 Ma is associated with formation and deformation of quartz–sillimanite nodules that recorded an increment of vertical shortening and E–NE extension; and

(3) crystallization of the post-kinematic Ourtigas leucogranite at 298 ± 2 Ma was coeval with (i) cooling of the dome gneiss and granite, (ii) shearing that developed along the northern and southern margins of the dome, and (iii) activity on the eastern detachment system.
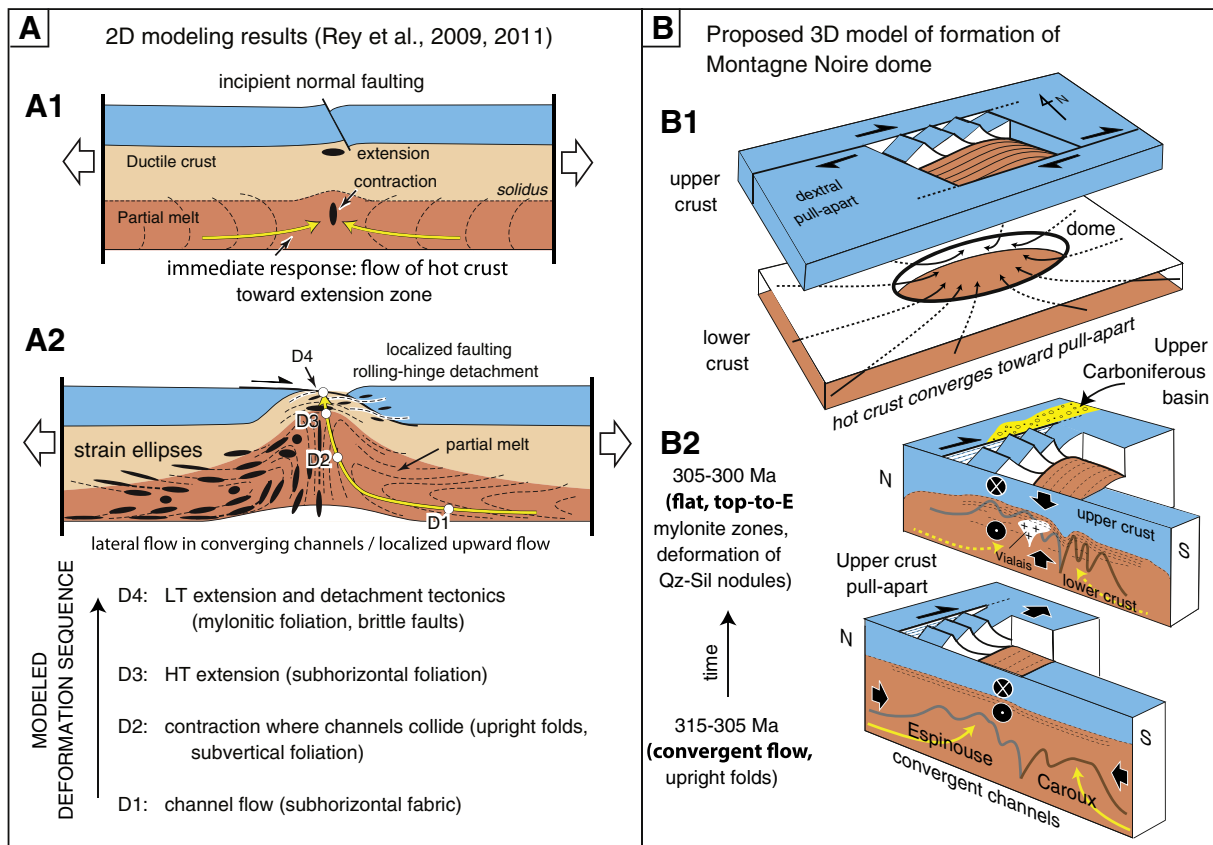
Fig. 10. A) Results of 2D modeling of extension of hot crust, showing that convergent flow at depth and extension in upper crust are coeval (A1). During steady extension at the boundaries, channels converge beneath the zone of upper crust and form a double dome of foliation (A2); lower crust material records a deformation sequence that includes flow in horizontal channel (D1), horizontal shortening with upright folds and vertical foliation that form during decompression and upward flow (D2), vertical shortening (horizontal fabric) that develop during extension beneath the upper crust (D3), and low-T/brittle deformation during latest exhumation (D4). B) Proposed 3D model for the formation and exhumation of the Montagne Noire axial zone. Low-viscosity crust converges toward the zone of upper crust extension (pull-apart structure in strike–slip corridor) (B1). In the Axial Zone of the Montagne Noire (B2) rocks record high-temperature flow of crust (315–305 Ma) under partial melting conditions and development of flat foliation that is progressively overprinted by vertical foliation and upright folds during decompression. As rocks are progressively exhumed, they enter the field of extension and develop flat fabrics that overprints earlier structures (quartz–sillimanite nodules recorded this increment of strain). At the eastern termination of the Montagne Noire dome, top-to-the-E or -NE extensional fabric is developed around 305–300 Ma during and after crystallization of the Vialais granite.
A, after P.F. Rey et al. (2009a,b), Rey et al. (2011a,b).

These results are inconsistent with the Montagne Noire dome's having been emplaced during regional contraction and nappe emplacement (e.g., Matte et al., 1998; Faure et al., 2010, 2014). Although our results do not date the beginning of anatexis in the Montagne Noire, they place synkinematic monazite crystallization and anatectic granite emplacement at 310–300 Ma, 20 m.y. after the proposed age of the high-temperature–low-pressure metamorphic event (333–326 Ma, Faure et al., 2014), and certainly well after the contractional stage that preceded it.

Therefore, our results contradict models that invoke the main contractional event (crustal thickening, nappe emplacement, and HP–LT metamorphism) in the French Massif Central to explain the geology of the Montagne Noire. Instead our geochronology results suggest a close temporal association, during the Late Carboniferous, between contractional and extensional structures, as would be the case in a strike–slip (or transpressional/transtensional) zone in which folding and extension structures coexist (e.g., Fossen et al., 2013). However, folds are quite tight in the Axial Zone of the Montagne Noire, and the amount of shortening appears higher than would be expected from a wrenching. Therefore an additional contractional component in a transpression zone could account for the localized shortening observed in the Montagne Noire.

Alternatively, we propose that this shortening was in fact coeval with extension in the upper crust and can be explained by the flow of low-viscosity lower crust that converged toward a zone of extension in the upper crust (Fig. 10). This interpretation relies on the geodynamic principle that low-viscosity mid- or lower crust can flow readily toward a zone of extension/dilation in the upper crust (Wdowinski and Axen, 1992; P.F. Rey et al., 2009; P. Rey et al., 2009). We argue that the Montagne Noire dome formed late in the Variscan orogeny and was related to local extension between two dextral strike–slip zones (pull-apart structure, Fig. 10B), as proposed by Echtler and Malavieille (1990). The timing of this strike–slip/transtensional system was recently documented in the Flanc Sud nappes (Doublier et al., 2014). Extension in a dilational jog solicited flow of partially molten crust that was drawn toward the pull-apart (Fig. 10B$_1$). Dynamic modeling in 2D shows that the low-viscosity crust converges effectively toward the extension zone and produces a double dome as well as contraction structures beneath it (Fig. 10A$_1$). Material rises to fill the opening created by the upper crust pull-apart, forming a double dome and going through a sequence of deformation that involves contractional strain followed by extensional strain as the low-viscosity material moves up and enters the extensional detachment system. This sequence of deformation during melt-present flow followed by solid-state high-temperature crystallization, then low-temperature deformation and recrystallization in extensional mylonite zones, is a first-order characteristic of the Montagne Noire evolution (Espinouse and Caroux double dome, melt-present upright folding, subhorizontal mylonitic overprint; Fig. 2E). Geochronology results (this study; Franke et al., 2011) indicate that dome development and contractional structures in the present-day

exposures of the Montagne Noire occurred around 315–305 Ma (Fig. 10B₂).

The onset of extensional deformation in the Montagne Noire rocks at present-day exposure levels is tracked by our new results for the age of the Vialais granite. When the Vialais granite crystallized at ~303 Ma, the structural level at which the granite was emplaced was deforming in extension (Fig. 10B₂), as indicated by the vertical shortening and E–NE directed stretching recorded by quartz–sillimanite nodules, and also suggested by the tension gash shape of the Vialais granite body itself (Fig. 2). Continued extension juxtaposed anatectic dome rocks and detachment mylonites that decapitated and transposed the upper levels of the dome eastern region, resulting in a sharp metamorphic gradient from migmatite to mylonite between the core and the carapace of the domes (Van den Driessche and Brun, 1989, 1992). The last melt crystallized in the dome at ~298 Ma (i.e. Ourtigas leucogranite); at that time the last dextral–normal mylonite zones around the dome were still active. The whole system cooled through the biotite and muscovite argon closure temperatures over the next few million years (Maluski et al., 1991; Franke et al., 2011).

8. Partial melting in the Montagne Noire and general conclusions

Partial melting of the orogenic crust started during convergence and crustal thickening at ~330 Ma in some areas of the Variscan orogen (Faure et al., 2010). It is becoming clear, however, that high-temperature metamorphism and emplacement and crystallization of anatectic bodies to shallow crustal levels did not occur until about 315–300 Ma in the Montagne Noire. The Late Carboniferous age for the Vialais granite is consistent with many of the ages attributed to anatectic processes in the Variscan belt of the Massif Central. In the Velay area (Cévennes) a late Variscan event involving migmatite and associated cordierite granite emplacement has been dated at 310–295 Ma (Mougeot et al., 1997; Ledru et al., 2001; Montel et al., 2002). Ages obtained on migmatite in the southern part of the Velay dome range from 330 to 300 Ma (Mougeot et al., 1997; Bé Mezème et al., 2006). These data have been interpreted to indicate the onset of partial melting following crustal thickening (~330 Ma) and crystallization of the last melt during gravitational collapse of thickened crust 30 My later (Vanderhaeghe et al., 1999; Ledru et al., 2001).

However, unlike other regions of the Massif Central where late Carboniferous emplacement of migmatite domes has been associated with conductive heating during and after crustal thickening, the origin of crustal melting in the Montagne Noire and other external zones is enigmatic (Franke et al., 2011) because this segment of the Variscan belt was in a foreland position relative to the Variscan plateau to the north. In neighboring external zones, granites from the Cévennes (Brichau et al., 2008) and from the Pyrenees (Respaut and Lancelot, 1983; Paquette et al., 1997; Roberts et al., 2000; Maurel et al., 2004; Gleizes et al., 2006) display similar late Carboniferous ages. Therefore, the source of heat was probably not caused by thermal relaxation of thickened crust.

Late Variscan tectonics is characterized by large strike–slip systems that controlled the formation and filling of Stephanian basins; these basins contain volcanic deposits that were sourced in both the crust and the mantle (e.g. Bruguier et al., 2003). Lithosphere-scale strike–slip fault zones can be the location of significant heat and material transfer from the mantle to the crust and may be responsible for elevating the geotherm (Leloup and Kienast, 1993) and melting the crust. Strike–slip fault zones also form pull-apart structures that localize extension and create basins but may also attract partially molten crust to form migmatite domes like in the Montagne Noire, as we propose in this paper.

Whatever process drove partial melting, hot orogenic crust flowed to form the Espinouse and Caroux sub-domes at ~315–300 Ma. Our results for the age of monazite crystallization in the Héric augen gneiss (~308 Ma) and the Vialais granite (~303 Ma), coupled with the deformation fabrics recorded in the augen gneiss and the quartz–sillimanite nodules, suggest that dome rocks moved upward into a zone of crustal extension and underwent a sequence of contraction to extension during flow and exhumation at about 315–300 Ma. During that time interval, contraction and extension were likely coeval, and dome rocks moved from the contraction domain upward into the extension domain.

Acknowledgments

Appendix A. Supplementary data

Supplementary data to this article can be found online at http://dx.doi.org/10.1016/j.tecto.2014.12.002.

References

Arthaud, F., 1970. Etude tectonique et microtectonique comparée de deux domaines hercyniens: les nappes de la Montagne Noire (France) et l'anticlinorium de l'Iglesiente (Sardaigne). Université des Sciences et Techniques du Languedoc, p. 175.

Bard, J.P., Rambeloson, R., 1973. Métamorphisme plurifacial et sens de variation du degré géothermique durant la tectogenèse hercynienne dans la partie orientale de la zone axiale de la Montagne Noire (massif du Caroux, sud du Massif Central français). Bull. Soc. Geol. Fr. 15, 579–586.

Bé Mezème, E., Cocherie, A., Faure, M., Legendre, O., Rossi, P., 2006. Electron microprobe monazite geochronology: a tool for evaluating magmatic age domains. Examples from the Variscan French Massif Central. Lithos 87, 276–288.

Beaud, F., 1985. Etude structurale de la Zone Axiale orientale de la Montagne Noire (Sud du Massif Central Français). Détermination des mécanismes de déformation. Relation avec les nappes du Versant Sud: Thèse 3ème cycle. Université des Sciences et Techniques du Languedoc, Montpellier (191 pp.).

Beaumont, C., Jamieson, R.A., Nguyen, M.H., Lee, B., 2001. Himalayan tectonics explained by extrusion of a low-viscosity crustal channel coupled to focused surface denudation. Nature 414, 738–742.

Beaumont, C., Nguyen, M.H., Jamieson, R.A., Ellis, S., 2006. Crustal flow modes in large hot orogens. In: Law, R.D., Searle, M.P., Godin, L. (Eds.), Channel Flow, Ductile Extrusion and Exhumation in Continental Collision Zones. Geological Society, London, Special Publication 268, pp. 91–145.

Bogdanoff, S., 1970. Contribution à l'étude géologique de l'extrémité orientale de la zone axiale granite-gneissique de la Montagne Noire, Thèse 3° cycle. Univ. Orsay (91 pp.).

Bogdanoff, S., Donnot, M., Ellenberger, F., 1984. Carte géologique de Bédarieux. Carte géologique de la France au 1/50000, no. 988.

Brichau, S., Respaut, J.P., Monié, P., 2008. New age constraints on emplacement of the Cévenols granitoids, South French Massif Central. Int. J. Earth Sci. (Geol. Rundsch.) 97, 725–738.

Brown, M., 1994. The generation, segregation, ascent and emplacement of granite magma — the migmatite-to-crustally-derived-granite connection in thickened orogens. Earth-Sci. Rev. 36 (1–2), 83–130.

Brown, M., 2001. Crustal melting and granite magmatism: key issues. Phys. Chem. Earth Solid Earth Geod. 26 (4–5), 201–212.

Bruguier, O., Becq-Giraudon, J.F., Champenois, M., Deloule, E., Ludden, J., Mangin, D., 2003. Application of in situ zircon geochronology and accessory phase chemistry to constraining basin development during post-collisional extension: a case study from the French Massif Central. Chem. Geol. 201, 319–336.

Brun, J.P., Van Den Driessche, J., 1994. Extensional gneiss domes and detachment fault systems: structure and kinematics. Bull. Soc. Geol. Fr. 165 (6), 519–530.

Brun, J.P., Van Den Driessche, J., 1996. Réponse à observations et remarques sur l'article "Extensional gneiss domes and detachment fault systems/structure and kinematics (Brun, J.P., Van Den Driessche, J., 1994, Bull. Soc. Géol. Fr. 165 (6), 519–530)". Bull. Soc. Géol. Fr. 167 (2), 295–302.

Brunel, M., Lansigu, C., 1997. Deformation and kinematics of emplacement of the axial dome of the Montagne Noire: implications of quartz–sillimanite nodule attitudes (French massif central). C. R. Acad. Sci. Paris II 325 (7), 517–523.

Cocherie, A., Baudin, T., Autran, A., Guerrot, C., Fanning, M., Laumonier, B., 2005. U–Pb zircon (ID-TIMS and SHRIMP) evidence for the early Ordovician intrusion of metagranites in the late Proterozoic Canaveilles Group of the Pyrenees and the Montagne Noire (France). Bull. Soc. Geol. Fr. 176, 269–282.

Demange, M., 1982. Etude géologique du Massif de l'Agout, Montagne Noire, France. A geologic study of the Agout Massif, Montagne Noire, France, Doctoral, Univ. Paris VI.

Demange, M., 1985. The eclogite-facies rocks of the Montagne Noire, France. Chem. Geol. 50, 173–188.

Demange, M., 1999. Evolution tectonique de la Montagne Noire: un modèle en transpression. C. R. Acad. Sci. Paris 329, 823–829.

Den Tex, E., 1975. Thermally mantled gneiss domes; the case for convective heat flow in more or less solid orogenic basement. In: Borradaile, G.J., Ritsema, A.R., Rondeel, H.E.,

Simon, O.J. (Eds.), Geodynamics Project, Scientific Report. North-Holland Publ. Co., Amsterdam, Netherlands.

Doublier, M.P., Potel, S., Wemmer, K., 2014. The tectono-metamorphic evolution of the very low-grade hanging wall constrains two stage gneiss dome formation in the Montagne Noire example (S-France). J. Metamorph. Geol. http://dx.doi.org/10.1111/jmg.12111.

Ducrot, J., Lancelot, J.R., Reille, J.L., 1979. Datation en Montagne Noire d'un témoin d'une phase majeure d'amincissement crustal caractéristique de l'Europe prévarisque. Age of a major phase of crustal thinning characteristic of Prevariscan Europe determined in the Montagne Noire region. Bull. Soc. Geol. Fr. 21 (4), 501–505.

Echtler, H., Malavieille, J., 1990. Extensional tectonics, basement uplift and Stephano-Permian collapse basin in a late Variscan metamorphic core complex (Montagne Noire, southern Massif Central). Tectonophysics 177, 125–138.

Engel, W., Feist, R., Franke, W., 1980. Le Carbonifère anté-stéphanien de la Montagne Noire: rapports entre mise en place des nappes et sédimentations. Bull. BRGM 2, 341–389.

Faure, M., Cottereau, N., 1988. Données cinématiques sur la mise en place du dôme migmatitique carbonifère moyen de la zone axiale de la Montagne Noire (Massif Central, France). C. R. Acad. Sci. Paris 307, 1787–1794.

Faure, M., Cocherie, A., Bé Mézène, E., Charles, N., Rossi, P., 2010. Middle Carboniferous crustal melting in the Variscan belt: new insights from U–Th–Pbtot monazite and U–Pb zircon ages of the Montagne Noire Axial Zone (southern French Massif Central). Gondwana Res. 18, 653–673.

Faure, M., Cocherie, A., Gaché, J., Esnault, C., Guerrot, C., Rossi, Ph., Wei, Lin, Qiuli, Li, 2014. Middle Carboniferous intracontinental subduction in the outer zone of the Variscan belt (Montagne Noire Axial Zone, French Massif Central): multimethod geochronological approach of polyphase metamorphism. Geol. Soc. Lond. Spec. Publ. http://dx.doi.org/10.1144/SP405.2.

Feist, R., Galtier, J., 1985. Découverte de flores d'âge namurien probable dans le flysch à olistolithes de Cabrières (Hérault). Implications sur la durée de la sédimentation synorogénique dans la Montagne Noire (France Méridionale). C. R. Acad. Sci. Paris 300, 207–212.

Fossen, H., Teyssier, C., Whitney, D.L., 2013. Transtensional folding. J. Struct. Geol. 56, 89–102.

Franke, W., Doublier, M.P., Klama, K., Potel, S., Wemmer, K., 2011. Hot metamorphic core complex in a cold foreland. Int. J. Earth Sci. (Geol. Rundsch.) http://dx.doi.org/10.1007/s00531-010-0512-7.

Gèze, B., 1949. Etude géologique de la Montagne Noire et des Cévennes méridionales. Soc. Géol. Fr. Mém. 62, 1–125.

Gleizes, G., Crevon, G., Astrat, A., Barbey, P., 2006. Structure, age and mode of emplacement of the Hercynian Bordère-Louron pluton (Central Pyrenees, France). Int. J. Earth Sci. (Geol. Rundsch.) 95, 1039–1052.

Gordon, S.M., Whitney, D.L., Teyssier, C., Grove, M., Dunlap, W.J., 2008. Timescales of migmatization, melt crystallization, and cooling in a Cordilleran gneiss dome: Valhalla complex, southeastern British Columbia. Tectonics 27, 4. http://dx.doi.org/10.1029/2007TC002103.

Gordon, S.M., Grove, M., Whitney, D.L., Schmitt, A.K., Teyssier, C., 2009. Fluid–rock interaction in orogenic crust tracked by zircon depth profiling. Geology 37, 735–738.

Hanchar, J.M., Miller, C.F., 1993. Zircon zonation patterns as revealed by cathodoluminescence and backscattered electron images: implication for interpretation of complex crustal histories. Chem. Geol. 110, 1–13.

Hartmann, L.A., Santas, J.O.S., 2004. Predominance old high Th/U, magmatic zircon in Brazilian shield sandstones. Geology 32, 73–76.

Horstwood, M.S.D., Foster, G.L., Parrish, R.R., Noble, G.M., 2003. Commun-Pb corrected in situ U–Pb accessory mineral geochronology by LA-MC-ICP-MS. J. Anal. At. Spectrom. 18, 837–846.

Hoskin, P.W.O., 2000. Patterns of chaos: fractal statistics and the oscillatory chemistry of zircon. Geochim. Cosmochim. Acta 64, 1905–1923.

Hoskin, P.W.O., Black, L.P., 2000. Metamorphic zircon formation by solid-state recrystallization of protolith igneous zircon. J. Metamorph. Geol. 18, 423–439.

Hurai, V., Paquette, J.L., Huraiovà, M., Konecny, P., 2010. U–Th–Pb geochronology of zircon and monazite from syenite and pincinite xenoliths in Pliocene alkali basalts of the intra-carpathian back-arc basin. J. Volcanol. Geotherm. Res. 198, 275–287.

Jackson, S.E., Pearson, N.J., Griffin, W.L., Belousova, E.A., 2004. The application of laser ablation-inductively coupled plasma mass spectrometry to in situ U–Pb zircon geochronology. Chem. Geol. 211, 47–69.

Jaffey, A.H., Flynn, K.F., Glendenin, L.E., Bentley, W.C., Essling, A.M., 1971. Precision measurement of half-lives and specific activities of 235U and 238U. Phys. Rev. C4, 1889–1906.

Krogh, T.E., 1982. Improved accuracy of U/Pb zircon ages by the creation of more concordant systems using air abrasion technique. Geochim. Cosmochim. Acta 46, 637–649.

Kruckenberg, S.C., Whitney, D.L., Ferré, E., Chapman, A., Vanderhaeghe, O., 2008. Compatibility of deformation between upper crust and flowing partially molten crust in "hot" orogens, EGU 2008, Vienna. Geophysical Research Abstracts vol. 10.

Kruckenberg, S.C., Vanderhaeghe, O., Ferré, E.C., Teyssier, C., Whitney, D.L., 2011. Flow of partially molten crust and the internal dynamics of a migmatite dome: Naxos, Greece. Tectonics. http://dx.doi.org/10.1029/2010TC002751.

Ledru, P., Courrioux, G., Dallain, C., Lardeaux, J.M., Montel, J.M., Vanderhaeghe, O., Vitel, G., 2001. The Velay dome (French Massif Central): melt generation and granite emplacement during orogenic evolution. Tectonophysics 342, 207–237.

Leloup, P.H., Kienast, J.R., 1993. High-temperature metamorphism in a major strike–slip shear zone—the Ailao Shan River, People's Republic of China. Earth Planet. Sci. Lett. 118 (1–4), 213–234.

Loueyit, C.J., 1978. Etude pétrographique des Monts de l'Espinouse dans la zone axiale de la Montagne Noire (Massif Central français). Mém. DEA, Univ. Sciences et Techniques du Languedoc (57 pp.).

Ludwig, K.R., 1993. Pbdat: a computer program for processing Pb–U–Th isotope data, version 1.24. United States Geological Survey Open-file Reportpp. 88–542.

Ludwig, K.R., 2001. User manual for Isoplot/Ex rev. 2.49. A geochronological toolkit for Microsoft Excel. Berkeley Geochronology Center Special Publication 1a, pp. 1–56.

Malavieille, J., Konstantinoskaya, E., 2010. Impact of surface processes on the growth of orogenic wedges: insights from analog models and case studies. Geotectonics 44 (6), 541–558.

Maluski, H., Costa, S., Echtler, H., 1991. Late Variscan tectonic evolution by thinning of earlier thickened crust: an 40Ar–39Ar study of the Montagne Noire, southern Massif Central, France. Lithos 26 (3–4), 287–304.

Mattauer, M., Laurent, Ph., Matte, Ph., 1996. Plissement hercynien synschisteux post-nappe et etirement subhorizontal dans le versant sud de la Montagne Noire (Sud du Massif Central, France). Post-nappe synschistose Hercynian folding and horizontal stretching in the southern side of Montagne Noire, southern Central Massif, France. C. R. Acad. Sci. II 322 (4), 309–315.

Matte, Ph., 2007. Variscan thrust nappes detachments and strike–slip faults in the French Massif Central: interpretation of the lineations. Geol. Soc. Am. Mem. 200, 319–402.

Matte, Ph., Lancelot, J., Mattauer, M., 1998. La Zone axiale hercynienne de la Montagne Noire n'est pas un "metamorphic core complex" extensif mais un anticlinal post-nappe à coeur anatectique. Geodin. Acta (Paris) 11 (1), 13–22.

Maurel, O., Respaut, J.P., Monié, P., Arnaud, N., Brunel, M., 2004. U–Pb emplacement and 40Ar/39Ar cooling ages of the eastern Mont-Louis granite massif (Eastern Pyrenees, France). C. R. Geosci. Acad. Sci. Paris 336, 1091–1098.

Montel, J.M., Bouloton, J., Veschambre, M., Pellier, C., Ceret, K., 2002. Ages stéphaniens des microgranites du Velay (Massif Central français). Géol. Fr. 1, 15–20.

Mougeot, R., Respaut, J.P., Ledru, P., Marignac, C., 1997. U–Pb chronology on accessory minerals of the Velay anatectic dome (French Massif Central). Eur. J. Mineral. 9, 141–156.

Müller, W., Shelley, M., Miller, P., Broude, S., 2009. Initial performance metrics of a new custom-designed ArF excimer La-ICPMS system coupled to a two-volume laser-ablation cell. J. Anal. At. Spectrom. 24, 209–214.

Nicolas, A., Bouchez, J.L., Blaise, J.L., Poirier, J.P., 1977. Geological aspects of deformation in continental shear zones. Tectonophysics 42, 55–73.

Paquette, J.L., Pin, C., 2001. A new miniaturized extraction chromatography method for precise U–Pb zircon geochronology. Chem. Geol. 176 (1–4), 311–319.

Paquette, J.L., Tiepolo, M., 2007. High resolution (5microm) U–Th–Pb isotope dating of monazite with excimer laser ablation (ELA-ICPMS). Chem. Geol. 240, 22–237.

Paquette, J.L., Gleizes, G., Leblanc, D., Bouchez, J.L., 1997. Le granite de Bassiès (Pyrenées): un pluton syntectonique d'âge westaphalien. Géochronologie U–Pb sur zircons. C. R. Acad. Sci. Paris 324, 387–392.

Pidgeon, R.T., 1992. Recrystallization of oscillatory zoned zircon: some geochronological and petrological implications. Contrib. Mineral. Petrol. 110 (4), 463–472.

Pitra, P., Poujol, M., Van Den Driessche, J., Poilvet, J.–C., Paquette, J.L., 2012. Early Permian extensional shearing of an Ordovician granite: the Saint-Eutrope "C/S-like" orthogneiss (Montagne Noire, French Massif Central). C. R. Geosci. http://dx.doi.org/10.1016/j.crte.2012.06.002.

Poilvet, J.C., Poujol, M., Pitra, P., Van Den Driesssche, J., Paquette, J.L., 2011. The Montalet granite, Montagne Noire, France: an Early Permian syn-extensional pluton as evidenced by new U–Th–Pb data on zircon and monazite. C. R. Geosci. 343, 454–461. http://dx.doi.org/10.1016/j.crte.2011.06.002.

Respaut, J.P., Lancelot, J.R., 1983. U–Pb dating on zircons and monazites of the synmetamorphic emplacement of the Ansignan charnockite (Agly Massif, France). Neues Jb. Mineral. Abh. 147, 21–34.

Rey, P., Vanderheaghe, O., Teyssier, C., 2001. Gravitational collapse of continental crust: definition, regimes, and modes. Tectonophysics 342, 435–449. http://dx.doi.org/10.1016/S0040-1951(01)00174-3.

Rey, P.F., Teyssier, C., Wittney, D.L., 2009a. The role of partial melting and extensional strain rates in the development of metamorphic core complexes. Tectonophysics 477, 133–144.

Rey, P., Teyssier, C., Whitney, D.L., 2009b. Crustal melting and core complex dynamics. Geology 37 (5), 391–394.

Rey, P.F., Teyssier, C., Kruckenberg, S.C., Whitney, D.L., 2011a. Viscous collision in channel explains double domes in metamorphic core complexes. Geology 39 (4), 387–390.

Rey, P.F., Teyssier, C., Kruckenberg, S.C., Whitney, D.L., 2011b. Viscous collision in channel explains double domes in metamorphic core complexes. Geology, Forum Reply, October, 2012.

Roberts, M.P., Pin, C., Clemens, J.D., Paquette, J.L., 2000. Petrogenesis of mafic to felsic plutonic rock associations: the calc-alkaline Quérigut complex, French Pyrenees. J. Petrol. 41, 809–844.

Roger, F., Respaut, J.P., Brunel, M., Matte, Ph., Paquette, J.L., 2004. Première datation U–Pb des orthogneiss oeillés de la zone axiale de la Montagne Noire (Sud du Massif Central): nouveaux témoins du magmatisme ordovicien dans la chaîne varisque. C. R. Geosci. Acad. Sci. Paris 336, 19–28.

Roger, F., Maluski, H., Lepvrier, C., Vu Van, T., Paquette, J.L., 2012. LA-ICPMS zircons U/Pb dating of Permo-Triassic and Cretaceous magmatisms in Northern Vietnam — geodynamical implications. J. Asian Earth Sci. 48, 72–82. http://dx.doi.org/10.1016/j.jseaes.2011.12.012.

Rosenberg, C.L., Handy, M.R., 2005. Experimental deformation of partially melted granite revisited: implications for the continental crust. J. Metamorph. Geol. 23, 19–28. http://dx.doi.org/10.1111/j.1525-1314.2005.00555.x.

Schuiling, R.D., 1960. Le dome gneissique de l'Agoût (Tarn et Hérault), Mémoires de la Sociéte Géologique de France. Nouv. Ser. 39 (91), 59.

Schuiling, R.D., 1963. Some remarks concerning the scarcity of retrograde vs. progressive metamorphism, Geologie en Mijnbouw. Neth. J. Geosci. 42 (5), 177–179.

Schuiling, R.D., Widt, J., 1962. Sur la génèse du dôme gneissique de l'Agoût (Dépts Tarn et Hérault). Geol. Mijnb. Ned. 41, 321–326.

Soula, J.C., Debat, P., Brusset, S., Bessiere, G., Christophoul, F., Deramond, J., 2001. Thrust-related, diapiric, and extensional doming in a frontal orogenic wedge: example of the Montagne Noire, southern French Hercynian Belt. J. Struct. Geol. 23 (11), 1677–1699.

Stacey, J.S., Kramers, J.D., 1975. Approximation of terrestrial lead isotope evolution by a two-stage model. Earth Planet. Sci. Lett. 26, 207–221.

Steiger, R.H., Jäger, E., 1977. Subcommission on geochronology: convention on the use of decay constants in geo- and cosmochronology. Earth Planet. Sci. Lett. 36, 359–362.

Teyssier, C., Whitney, D.L., 2002. Gneiss domes and orogeny. Geology 30, 1139–1142. http://dx.doi.org/10.1130/0091-7613(2002)030.

Teyssier, C., Ferré, E.C., Whitney, D.L., Norlander, B., Vanderhaeghe, O., Parkinson, D., 2005. Flow of partially molten crust and origin of detachments during collapse of the Cordilleran orogen. In: Bruhn, D., Burlini, L. (Eds.), High-strain Zones: Structure and Physical Properties. Geological Society of London Special Publication 245, pp. 39–64. http://dx.doi.org/10.1144/GSL.SP.2005.245.01.03.

Thompson, P.H., Bard, J.P., 1982. Isograds and mineral assemblages in the Eastern Axial Zone, Montagne Noire (France): implications for temperature gradients and P/T history. Can. J. Earth Sci. 19 (1), 129–143.

Van Den Driessche, J., Brun, J.P., 1989. Kinematic model of late Paleozoic extensional tectonics in the southern French massif central. C. R. Acad. Sci. II 309 (16), 1607–1613.

Van Den Driessche, J., Brun, J.P., 1992. Tectonic evolution of the Montagne Noire (French Massif Central): a model of extensional gneiss dome. Geodin. Acta 5, 85–99.

Van Den Driessche, J., Pitra, P., 2012. Viscous collision in channel explains double domes in metamorphic core complexes. Geology 40 (10), E279. http://dx.doi.org/10.1130/G32727C.1.

Vanderhaeghe, O., 2009. Migmatites, granites and orogeny: flow modes of partially-molten rocks and magmas associated with melt/solid segregation in orogenic belts. Tectonophysics 477, 119–134. http://dx.doi.org/10.1016/j.tecto.2009.06.021.

Vanderhaeghe, O., 2012. The thermal–mechanical evolution of crustal orogenic belts at convergent plate boundaries: a reappraisal of the orogenic cycle. J. Geodyn. 56–57, 124–145. http://dx.doi.org/10.1016/j.jog.2011.10.004.

Vanderhaeghe, O., Teyssier, C., 2001. Partial melting an flow of orogens. Tectonophysics 342, 451–472.

Vanderhaeghe, O., Burg, J.-P., Teyssier, C., 1999. Exhumation of migmatites in two collapsed orogens. In: Ring, U., Brandon, M.T., Lister, G.S., Willet, S.D. (Eds.), Exhumation Processes: Normal Faulting, Ductile Flow and Erosion. Geol. Soc., London, Spec. Publ. 154, pp. 181–204.

Vavra, G., Gebauer, D., Schmid, R., Compston, W., 1996. Multiple zircon growth and re-crystallization during polyphase Late Carboniferous to Triassic metamorphism in granulites of the Ivrea Zone (Southern Alps): an ion microprobe (SHRIMP) study. Contrib. Mineral. Petrol. 122, 337–358.

Wdowinski, S., Axen, G.J., 1992. Isostatic rebound due to tectonic denudation: a viscous low model of a layered lithosphere. Tectonics 11, 303–315.

Whitney, D.L., Teyssier, C., Vanderhaeghe, O., 2004. Gneiss Domes and Crustal Flow. In: Whitney, D.L., et al. (Eds.), Gneiss domes in orogeny. Geological Society of America Special Paper 380, pp. 15–33.

Whitney, D.L., Teyssier, C., Rey, P., Buck, W.R., 2013. Continental and oceanic core complexes. Geol. Soc. Am. Bull. 125 (3–4), 273–298. http://dx.doi.org/10.1130/B30754.1.

Williams, I.S., Claesson, S., 1987. Isotopic evidence for the Precambrian provenance and Caledonian metamorphism of high grade paragneiss from the Seve Nappes Scandinavian Caledonides. Contrib. Mineral. Petrol. 97, 205–217.